



This is a repository copy of *Discontinuous Galerkin simulator of shallow vortical flow with turbulence*.

White Rose Research Online URL for this paper:

<https://eprints.whiterose.ac.uk/225534/>

Version: Accepted Version

---

**Article:**

Kesserwani, G. [orcid.org/0000-0003-1125-8384](https://orcid.org/0000-0003-1125-8384), Sun, X., Hajihassanpour, M. et al. (1 more author) (2025) Discontinuous Galerkin simulator of shallow vortical flow with turbulence. *Advances in Water Resources*. 104986. ISSN 0309-1708

<https://doi.org/10.1016/j.advwatres.2025.104986>

---

© 2025 The Authors. Except as otherwise noted, this author-accepted version of a journal article published in *Advances in Water Resources* is made available via the University of Sheffield Research Publications and Copyright Policy under the terms of the Creative Commons Attribution 4.0 International License (CC-BY 4.0), which permits unrestricted use, distribution and reproduction in any medium, provided the original work is properly cited. To view a copy of this licence, visit <http://creativecommons.org/licenses/by/4.0/>

**Reuse**

This article is distributed under the terms of the Creative Commons Attribution (CC BY) licence. This licence allows you to distribute, remix, tweak, and build upon the work, even commercially, as long as you credit the authors for the original work. More information and the full terms of the licence here:

<https://creativecommons.org/licenses/>

**Takedown**

If you consider content in White Rose Research Online to be in breach of UK law, please notify us by emailing [eprints@whiterose.ac.uk](mailto:eprints@whiterose.ac.uk) including the URL of the record and the reason for the withdrawal request.



[eprints@whiterose.ac.uk](mailto:eprints@whiterose.ac.uk)  
<https://eprints.whiterose.ac.uk/>

# Discontinuous Galerkin simulator of shallow vortical flow with turbulence

Georges Kesserwani<sup>1</sup>, Xitong Sun<sup>1a</sup>, Mahya Hajihassanpour<sup>1,\*b</sup>, Mohammad Kazem Sharifian<sup>1,c</sup>

<sup>1</sup>*Civil and Structural Engineering, University of Sheffield, Mappin St, Sheffield City Centre, Sheffield S1 3JD, UK*

## Abstract

Shallow vortical flow can often occur past (un)submerged topographies, prevailing in quasi-steady states with turbulence. Practically, vortical flow is represented by the two-dimensional (2D) Reynolds-Averaged Navier–Stokes equations, including the two-equation  $k-\varepsilon$  turbulent model (RANS- $k-\varepsilon$ ), and are commonly resolved by finite difference/volumes second-order accurate solvers. Such RANS- $k-\varepsilon$  solvers, in addition to needing a fine resolution, require adding artificial treatments—extrinsic (unlocalised) reconstructions of wet-dry fronts with slope-limiting—that can impact the vortical eddy predictions. The second-order discontinuous Galerkin (DG2) solver intrinsically integrates the wet-dry fronts and uses localised slope-limiting; resulting in an implicit large eddy simulator with the shallow water equations (DG2-SWE) that can only simulate uncompounded eddies. A novel DG2 solver of RANS- $k-\varepsilon$  (DG2-RANS- $k-\varepsilon$ ) is devised for simulating a wider range of vortical eddies, by: first, transforming the  $5 \times 5$  advective-diffusive RANS- $k-\varepsilon$  system into a  $13 \times 13$  advection-dominated system; second, extending the DG2 formulation to the  $13 \times 13$  system, with adaptation of its robustness treatments for the mean-flow variables; and, last, adding a new combination of stability/positivity-preserving treatments for turbulent-flow quantities. The DG2-RANS- $k-\varepsilon$  solver is evaluated for simulating five experimental benchmarks using coarse, medium and fine resolutions. Results show that DG2-RANS- $k-\varepsilon$  can reproduce compound eddies from the medium resolution, and that DG2-RANS (without  $k-\varepsilon$ ) can better reproduce laminar wakes. Using the medium resolution reduces runtimes by 7-fold and running on the GPU further reduce runtimes by 2-to-6-fold. The code, including simulation setup files, is open-source within a new release of the LISFLOOD-FP hydraulic modelling environment (<https://doi.org/10.5281/zenodo.7628739>), with documentation and demonstration videos ([https://www.seamlesswave.com/DG2\\_RANS](https://www.seamlesswave.com/DG2_RANS)).

**Keywords:** Depth-averaged Reynolds-Averaged Navier–Stokes; Two-equation  $k-\varepsilon$  turbulence model; Second-order Discontinuous Galerkin; Advective-diffusive formulation; Compound eddies; Laminar & turbulent flow.

\* Corresponding author at: Department of Civil and Structural Engineering, University of Sheffield, Sheffield S1 3JD, UK. E-mail address: [G.kesserwani@sheffield.ac.uk](mailto:G.kesserwani@sheffield.ac.uk) and [mahya.hhp@gmail.com](mailto:mahya.hhp@gmail.com)

<sup>a</sup> currently at: Dalian Maritime University, China

<sup>b</sup> currently at: Autodesk Ltd., Sheffield, UK

<sup>c</sup> currently at: Moody's RMS, Inc., London, UK

## 1. Introduction

In open-channels, shallow vortical flow can occur past (un)submerged topographies (Neary and Odgaard 1993; Lloyd and Stansby 1997a; 1997b; Bazin et al. 2017; Mignot and Brevis 2020)—(un)submerged hereafter refers to both scenarios of submerged and unsubmerged (channel-bed) topographies emerging. Shallow vortical flow mostly prevails in quasi-steady states with high turbulence (Babarutsi et al. 1989; Ninto and Garcia 1966; Shucksmith et al. 2010; Begnudelli et al. 2010; Jha and Bombardelli 2011; Pandey and Mohapatra 2023). Practically, the mathematical modelling of shallow vortical flow has often been based on the depth-averaged two-dimensional (2D) Reynolds-Averaged Navier–Stokes (RANS) equations, as a trade-off between computational efficiency and modelling accuracy (Hinterberger et al. 2007; Rodi 2017; Zou et al. 2023).

The RANS equations can be regarded as an extended form of the simpler 2D shallow water equations (SWE) that—in addition to the inviscid fluxes and the topography and friction source terms—further incorporates the viscous stresses and the turbulent stresses. These stresses include second-order derivative (diffusive) terms, adding kinematic viscosity effects and turbulent-flow velocity fluctuations onto the mean-flow (superimposing various eddy sizes). Following Boussinesq’s assumption, depth-averaged integration of the turbulent stresses can be achieved using the eddy-viscosity concept (Rastogi and Rodi 1978); which, following Rodi (1993), results in the popular  $k$ - $\epsilon$  turbulence closure model (Haun et al. 2011; Gorji et al. 2014; Zou et al. 2020; Zou et al. 2023). In the  $k$ - $\epsilon$  model,  $k$  and  $\epsilon$  denote the turbulence kinetic energy and the turbulence kinetic energy dissipation rate, respectively, which make up the turbulent-flow variables that must also be evolved in space and time. Therefore, two (turbulence) transport equations must be added to the three RANS equations, resulting in a  $5 \times 5$  system (5 equations and 5 unknowns) that will be, hereafter, referred to as RANS- $k$ - $\epsilon$ .

Second-order finite volume/difference methods were used to develop numerical RANS- $k$ - $\epsilon$  solvers for turbulent shallow flow simulations, with the most notable developments focused on robustness treatments due to wet-dry fronts occurring past the unsubmerged topographies (Wu 2004; Cea et al. 2007; Yu and Duan 2012; Ginting 2019; Ginting and Ginting 2019)—unlike in Abakouy et al. (2017) and Zhang et al. (2019) where the unsubmerged topographies (e.g., solid walls and blocks) are removed from the computational mesh. In Wu (2004), the wet-dry front treatments were corrected by a standard wall function (StWF) for simulating unsteady dam-break flow on initially-dry movable and erodible topographies. Cea et al. (2007) also appended their wet-dry front treatments with a StWF to correct the turbulent-flow variables (Toro and García-Navarro 2007), but also needed to add (artificial) non-local limiters to velocity and turbulent-flow quantities. In their results, Cea

et al. (2007) identified that the turbulent-flow velocity fluctuations are mostly noticeable in the simulation of compound eddies of various sizes. Following Wu (2004), Yu and Duan (2012) also adapted wet-dry front treatments (Liang and Marche 2009) into a finite volume RANS- $k-\varepsilon$  solver and compared it to the SWE solver counterpart for simulating various dam-break flows past (un)submerged topographies. Their findings suggest that the RANS- $k-\varepsilon$  solver only significantly improved the predictions in the highly-turbulent localities past the (un)submerged topographies. However, most of the studies did not explore more challenging quasi-steady flow problems that are dominated by continuously and periodically moving eddies past unsubmerged topographies, hinting at outstanding issues; mostly, related to ensuring stability and positivity for the turbulent-flow variables and to avoiding too fine resolutions due to the StWF (sensitive to the size of near-dry-wall computational cells: the wet cells, with at least one wet-dry front, adjacent to any dry cell representing unsubmerged topographies).

To overcome resolution limitations, Ginting (2019) adapted a scalable wall function (ScWF) in their RANS- $k-\varepsilon$  solver with wet-dry front treatments; and, Ginting and Ginting (2019) added further enhancements to ensure stable and positivity-preserving quasi-steady eddy predictions past unsubmerged topographies. Their enhancements consisted of adding (artificial) numerical viscosity into the advective fluxes and of using non-local (artificial) reconstructions of second-order accurate wet-dry fronts. Arguably, on the one hand, adding numerical viscosity magnifies the growth of numerical error dissipation (Komen et al. 2017), impacting the physical  $k-\varepsilon$  model's dissipation [e.g., manifesting in deviated predictions from the true eddy sizes (Ginting and Ginting 2019)]. This impact can be alleviated by using too fine resolutions, but this is usually avoided to keep realistic runtimes (Landman et al. 2008; Dairay et al. 2017). On the other hand, reconstructing second-order accurate wet-dry fronts invoke non-local variables, outside the true wet-dry front localities [e.g., causing false noises (Hou et al. 2013)], and thereby can impact eddy predictions (Macías et al. 2020). This impact is usually damped by nonlinear limiters (Cea et al. 2007; Ginting and Ginting 2019), which, unless localised, affect the discretisation of diffusive terms (Navas-Montilla et al. 2019).

In a second-order discontinuous Galerkin solver of the SWE (DG2-SWE): second-order accurate wet-dry front representations is inherent in local (cellwise) piecewise-planar approximations of the flow variables and the topography; and, the approximated flow variables are evolved (cellwise) using a locally-conservative advective DG2 formulation, with localised limiters (Wei and Xia 2024) that do not interfere with the wet-dry front treatments (Kesserwani and Liang 2012; Kesserwani et al. 2018). Compared to equally-accurate finite volume/difference formulation, the DG2 formulation is immune to magnified growth of numerical error

dissipation and to loosing accuracy and stability, despite a localised integration of wet-dry fronts and of second-order derivative terms (Landman et al. 2008; Sharifian et al. 2018; Ayog et al. 2021, Sec. 2.3). Because of these properties, the DG2-SWE solver can produce unrivalled simulations using unusually coarse resolutions [e.g., of velocity transients in unsteady flows (Kesserwani and Wang 2014; Ayog et al. 2021), and of spatial velocities in steady flows (past)over (un)submerged topographies (Kesserwani 2013)].

In the simulation of quasi-steady shallow vortical flow, the DG2-SWE solver can be used as an implicit large eddy simulator (Moura et al. 2017; Plata et al. 2018; Bergmann et al. 2019) of laminar wakes and of uncompounded turbulent eddies (Kesserwani et al. 2023; Sun et al. 2023). However, its use for this purpose is limited to selecting an abnormally coarse resolution—far larger than the turbulence length scale yet finer than the Characteristic Length ( $CL$ )—and avoiding turbulent flow simulation problems dominated by compound eddies (Kesserwani et al. 2023). This limitation motivates for the development of a new DG2 solver of the  $5 \times 5$  RANS- $k-\varepsilon$  system (DG2-RANS- $k-\varepsilon$ ) that can generally and reliably simulate a wider range of vortical eddies with turbulence, and despite the presence of (un)submerged topographies in the computational domain.

Existing studies partly developed DG2-RANS- $k-\varepsilon$  solvers, none yet focussed on quasi-steady shallow vortical flow simulations past (un)submerged topographies. Kärnä (2020) reported a stable and positivity-preserving DG2 discretisation of two-equation turbulence closure models (including  $k-\varepsilon$ ), but their solution was aimed to improve unsteady predictions for an ocean-scale DG2 simulator (Kärnä et al. 2018). Whereas, Lee (2021) addressed the DG2 discretisation of the second-order derivative terms (Miller et al. 2013) for a simple turbulence model in a  $3 \times 3$  RANS system, reporting water depth results without wet-dry problems.

A novel DG2-RANS- $k-\varepsilon$  solver is developed (Sec. 2) by: first, transforming the  $5 \times 5$  RANS- $k-\varepsilon$  system into a  $13 \times 13$  system that only involves advection-dominated derivative terms; second, extending the advective DG2-SWE formulation to solve the  $13 \times 13$  system, while adapting its robustness treatments for the mean-flow variables; and, last, adding a new combination of stability/positivity-preserving treatments for the turbulent-flow quantities to ensure reliable DG2-RANS- $k-\varepsilon$  simulations. The evaluation approach (Sec. 3) of the DG2-RANS- $k-\varepsilon$  solver is reported for five experimental quasi-steady flow benchmarks, with runtime analyses for parallel simulations on a multi-core Central Processing Unit (CPU, 10 threads) and a Graphics Processing Unit (GPU, V100 card). The simulated DG2-RANS- $k-\varepsilon$  and DG2-SWE velocity fields using coarse, medium and fine resolutions are qualitatively and quantitatively compared against measured velocity fields (Sec. 4), to then conclude on the practical usability of the DG2-RANS- $k-\varepsilon$  solver (Sec. 5).

## 2. Computational approach

The mathematical  $5 \times 5$  RANS- $k-\varepsilon$  system is presented (Section 2.1), while contrasting the excessively reduced complexity in the simpler DG2-SWE solver (Section 2.2). This system is transformed into a  $13 \times 13$  advection-dominated system solved by the advective DG2 formulation with various robustness treatments (Section 2.3), leading to the ‘‘DG2-RANS- $k-\varepsilon$  turbulent flow solver’’ or the ‘‘DG2-RANS laminar flow solver’’ (without  $k-\varepsilon$ ).

### 2.1. Governing equations: the $5 \times 5$ RANS- $k-\varepsilon$ system

The  $5 \times 5$  RANS- $k-\varepsilon$  system involves two coupled sets of equations (Cea et al. 2007; Vázquez-Cendón et al. 2009; Abakouy et al. 2017; Ginting 2019; Zhang et al. 2019; Ginting and Ginting 2019): the set of three mean-flow equations, for which the mean-flow variables are indexed with the subscript ‘‘mean’’; and, the set of two turbulence transport equations, for which the turbulent-flow variables are indexed with the subscript ‘‘turb’’. In a vectorial (conservative) form, the  $5 \times 5$  RANS- $k-\varepsilon$  system can be expressed as follows:

$$\frac{\partial \mathbf{U}}{\partial t} = -\frac{\partial \mathbf{F}}{\partial x} - \frac{\partial \mathbf{G}}{\partial y} + \frac{\partial \mathbf{F}_v}{\partial x} + \frac{\partial \mathbf{G}_v}{\partial y} + \mathbf{S} \quad \text{with} \quad (1)$$

$$\mathbf{U} = \begin{bmatrix} \mathbf{U}_{\text{mean}} \\ \mathbf{U}_{\text{turb}} \end{bmatrix}, \mathbf{F} = \begin{bmatrix} \mathbf{F}_{\text{mean}} \\ \mathbf{F}_{\text{turb}} \end{bmatrix}, \mathbf{G} = \begin{bmatrix} \mathbf{G}_{\text{mean}} \\ \mathbf{G}_{\text{turb}} \end{bmatrix}, \mathbf{F}_v = \begin{bmatrix} \mathbf{F}_{v\text{mean}} \\ \mathbf{F}_{v\text{turb}} \end{bmatrix}, \mathbf{G}_v = \begin{bmatrix} \mathbf{G}_{v\text{mean}} \\ \mathbf{G}_{v\text{turb}} \end{bmatrix} \text{ and } \mathbf{S} = \begin{bmatrix} \mathbf{S}_{\text{mean}} \\ \mathbf{S}_{\text{turb}} \end{bmatrix}$$

In Eq. (1),  $\partial$  is the partial derivative operator,  $t$  the time and  $(x, y)$  the Cartesian coordinates of position;  $\mathbf{U}$  is the vector including the flow variables;  $\mathbf{F}$  and  $\mathbf{G}$  are vectors including the inviscid fluxes in the  $x$ - and  $y$ -directions;  $\mathbf{F}_v$  and  $\mathbf{G}_v$  are vectors including the viscous fluxes in the  $x$ - and  $y$ -directions, respectively; and,  $\mathbf{S}$  is the vector including the source terms. Each of vectors  $\mathbf{U}$ ,  $\mathbf{F}$ ,  $\mathbf{G}$ ,  $\mathbf{F}_v$ ,  $\mathbf{G}_v$  and  $\mathbf{S}$  have five scalar components, with the first three components packed in the sub-vectors with the bolded subscript ‘‘mean’’, thus sub-indexed as ‘‘mean $_i$ ’’ (with  $i = 1, 2, 3$ ), as shown in Eq. (2) in which  $T$  is the transpose operator:

$$\begin{aligned} \mathbf{U}_{\text{mean}} &= (U_{\text{mean}_1}, U_{\text{mean}_2}, U_{\text{mean}_3})^T = (h, hu, hv)^T \\ \mathbf{F}_{\text{mean}} &= (F_{\text{mean}_1}, F_{\text{mean}_2}, F_{\text{mean}_3})^T = (hu, hu^2 + 0.5gh^2, huv)^T \\ \mathbf{G}_{\text{mean}} &= (G_{\text{mean}_1}, G_{\text{mean}_2}, G_{\text{mean}_3})^T = (hv, huv, hv^2 + 0.5gh^2)^T \\ \mathbf{F}_{v\text{mean}} &= (F_{v\text{mean}_1}, F_{v\text{mean}_2}, F_{v\text{mean}_3})^T = \left[ 0, 2h(D_m + D_t) \frac{\partial u}{\partial x} - \frac{2}{3}hk, h(D_m + D_t) \left( \frac{\partial u}{\partial y} + \frac{\partial v}{\partial x} \right) \right]^T \\ \mathbf{G}_{v\text{mean}} &= (G_{v\text{mean}_1}, G_{v\text{mean}_2}, G_{v\text{mean}_3})^T = \left[ 0, h(D_m + D_t) \left( \frac{\partial u}{\partial y} + \frac{\partial v}{\partial x} \right), 2h(D_m + D_t) \frac{\partial v}{\partial y} - \frac{2}{3}hk \right]^T \\ \mathbf{S}_{\text{mean}} &= (S_{\text{mean}_1}, S_{\text{mean}_2}, S_{\text{mean}_3})^T = \left( 0, -gh \frac{\partial z}{\partial x} + S_{f_x}, -gh \frac{\partial z}{\partial y} + S_{f_y} \right)^T \end{aligned} \quad (2)$$

The two remaining scalar components are packed in the sub-vectors with the bolded subscript ‘‘turb’’, thus sub-indexed as ‘‘turb $_i$ ’’ (with  $i = 1, 2$ ), as shown in Eq. (3):

$$\begin{aligned}
\mathbf{U}_{\text{turb}} &= (U_{\text{turb}_1}, U_{\text{turb}_2})^T = (hk, h\varepsilon)^T \\
\mathbf{F}_{\text{turb}} &= (F_{\text{turb}_1}, F_{\text{turb}_2})^T = (hku, h\varepsilon u)^T \\
\mathbf{G}_{\text{turb}} &= (G_{\text{turb}_1}, G_{\text{turb}_2})^T = (hkv, h\varepsilon v)^T \\
\mathbf{F}_{v\text{turb}} &= (F_{v\text{turb}_1}, F_{v\text{turb}_2})^T = \left[ h \left( D_m + \frac{D_t}{\sigma_k} \right) \frac{\partial k}{\partial x}, h \left( D_m + \frac{D_t}{\sigma_\varepsilon} \right) \frac{\partial \varepsilon}{\partial x} \right]^T \\
\mathbf{G}_{v\text{turb}} &= (G_{v\text{turb}_1}, G_{v\text{turb}_2})^T = \left[ h \left( D_m + \frac{D_t}{\sigma_k} \right) \frac{\partial k}{\partial y}, h \left( D_m + \frac{D_t}{\sigma_\varepsilon} \right) \frac{\partial \varepsilon}{\partial y} \right]^T \\
\mathbf{S}_{\text{turb}} &= (S_{\text{turb}_1}, S_{\text{turb}_2})^T = (T_{PV_1}, T_{PV_2})^T + (T_{Pb_1}, T_{Pb_2})^T + (T_{d_1}, T_{d_2})^T \text{ with} \\
(T_{PV_1}, T_{PV_2}) &= \left[ \min(2D_t \Gamma h, c_l \varepsilon h), \min \left( 2c_{\varepsilon 1} D_t \Gamma h \frac{\varepsilon}{k}, c_{\varepsilon 1} c_l h \frac{\varepsilon^2}{k} \right) \right] \\
(T_{Pb_1}, T_{Pb_2}) &= \left[ \min(c_k u_f^3, c_l \varepsilon h), c_\varepsilon \frac{u_f^4}{h} \right] \\
(T_{d_1}, T_{d_2}) &= \left( -h\varepsilon, -hc_{\varepsilon 2} \frac{\varepsilon^2}{k} \right)
\end{aligned} \tag{3}$$

In Eq. (2),  $\mathbf{U}_{\text{mean}}$  includes the three mean-flow variables, which are the water depth,  $h$  [m], and unit-width discharges,  $hu$  and  $hv$  [ $\text{m}^2 \text{s}^{-1}$ ], involving the velocity components  $u$  and  $v$  [ $\text{m s}^{-1}$ ] in  $x$ - and  $y$ -directions, respectively;  $\mathbf{F}_{\text{mean}}$  and  $\mathbf{G}_{\text{mean}}$  are the mean-flow inviscid fluxes in which  $g$  [ $\text{m s}^{-2}$ ] denotes the gravity constant;  $\mathbf{F}_{v\text{mean}}$  and  $\mathbf{G}_{v\text{mean}}$  are the mean-flow viscous fluxes in which  $D_m$  [ $\text{m}^2 \text{s}^{-1}$ ] is the kinematic viscosity,  $hk$  [ $\text{m}^3 \text{s}^{-2}$ ] is the turbulent-flow variable of the turbulent kinetic energy,  $k$  [ $\text{m}^2 \text{s}^{-2}$ ]; whereas,  $D_t$  [ $\text{m}^2 \text{s}^{-1}$ ] is the turbulent eddy-viscosity, incorporating turbulent-flow velocity fluctuations onto the mean-flow variables. As shown in Eqs. (4) and (5),  $D_t$  further involves the turbulent kinetic energy dissipation rate,  $\varepsilon$  [ $\text{m}^2 \text{s}^{-3}$ ], the multiplication of two strain-rate tensors  $\Gamma$  [ $\text{s}^{-1}$ ] and an empirical constant  $c_\mu = 0.09$ . Note that, all the empirical constants are selected to be the same as those used in other finite volume RANS- $k$ - $\varepsilon$  solvers (Cea 2005; Cea et al. 2006; Ginting 2019; Ginting and Ginting 2019).

$$\Gamma = \left( \frac{\partial u}{\partial x} \right)^2 + \left( \frac{\partial v}{\partial y} \right)^2 + \frac{1}{2} \left( \frac{\partial u}{\partial y} + \frac{\partial v}{\partial x} \right)^2 \tag{4}$$

$$D_t = \min \left( c_\mu \frac{k^2}{\varepsilon}, \frac{k}{3} \sqrt{\frac{2}{\Gamma}} \right) \tag{5}$$

$\mathbf{S}_{\text{mean}}$  includes the mean-flow source terms integrating channel-bed topographical slopes,  $\partial z / \partial x$  and  $\partial z / \partial y$ , where  $z$  [m] is the ground elevation at position  $(x, y)$ ; and the friction slopes,  $S_{f_x} = -c_f u \sqrt{u^2 + v^2}$  and  $S_{f_y} = -c_f v \sqrt{u^2 + v^2}$ , where  $c_f = gn_M^2 h^{-1/3}$  is a flow resistance term derived from the Manning friction formula, thereby approximating the vertical turbulent stresses (Gioia and Bombardelli 2001), and  $n_M$  is the Manning's coefficient of channel-bed roughness.

In Eq. (3),  $\mathbf{U}_{\text{turb}}$  includes the two turbulent-flow variables, consisting of  $hk$  and  $h\varepsilon$  [ $\text{m}^3 \text{s}^{-3}$ ];  $\mathbf{F}_{\text{turb}}$  and  $\mathbf{G}_{\text{turb}}$  are the turbulent-flow inviscid fluxes;  $\mathbf{F}_{v_{\text{turb}}}$  and  $\mathbf{G}_{v_{\text{turb}}}$  are the turbulent-flow viscous fluxes in which  $\sigma_k = 1$  and  $\sigma_\varepsilon = 1.31$  are empirical constants;  $\mathbf{S}_{\text{turb}}$  includes the turbulent-flow source terms that is made of the components:  $(T_{PV_i})_{i=1,2}$  of the production of turbulent kinetic energy involving the empirical constants  $c_l = 10$  and  $c_{\varepsilon 1} = 1.44$ ;  $(T_{Pb_i})_{i=1,2}$  of the turbulent production from the friction effects, involving the friction velocity  $u_f = [c_f(u^2 + v^2)]^{0.5}$ ,  $c_k = c_f^{-0.5}$  and  $c_\varepsilon = 3.6 c_{\varepsilon 2} c_\mu^{0.5} c_f^{-0.75}$  with  $c_\mu = 0.09$  and  $c_{\varepsilon 2} = 1.92$  being two empirical constants; and,  $(T_{d_i})_{i=1,2}$  of the production of turbulent kinetic energy dissipation rate.

## 2.2. DG2-SWE solver

The DG2-SWE solver uses the ‘‘slope-decoupled’’ advective DG2 formulation to solve the SWE (Kesserwani et al. 2018), which already includes accurate integration of wet-dry fronts, as they occur along steep bed-slopes of unsubmerged topographies, with stability-preserving integration of friction slopes (Ayog et al. 2021; Shaw et al. 2021). It is based on the formulation in Cockburn and Shu (2001), suited for solving advection-dominated partial differential equations (PDEs), to solve Eq. (2) with  $D_m = D_t = 0$ : by local (cellwise) DG2 approximations to each mean-flow variable (in  $\mathbf{U}_{\text{mean}}$ ) that are locally evolved by the associated component-wise spatial DG2 operator—including the discretisations of the gradients of the associated mean-flow inviscid flux component (in  $\mathbf{F}_{\text{mean}}$  and  $\mathbf{G}_{\text{mean}}$ ) and of the associated mean-flow source term component (in  $\mathbf{S}_{\text{mean}}$ ). By further adopting the slope-decoupled DG2 formulation to span the local DG2 approximations of the mean-flow variables and the ground elevation too, a robust well-balanced integrations of (un)submerged topographies becomes inherent in the local discrete spatial DG2 operators (Kesserwani et al. 2018; Kesserwani and Sharifian 2020).

Compared to the standard advective DG2 formulation, the slope-decoupled formulation is 2.6 time less costly, to evolve one mean-flow variable [defined cellwise by 3 degrees of freedom (Eq. 11)]. Hence, computationally, 9 cellwise degrees of freedom are required in the DG2-SWE solver to store/evolve the three components of the mean-flow variables, with a time-step,  $\Delta t$ , restricted by a Courant number ( $Cr$ ) of 0.3.

The DG2-SWE solver can be used as an implicit large eddy simulator (Moura et al. 2017; Kesserwani et al. 2023; Sun et al. 2023), by selecting an abnormally coarse resolution that is finer than the Characteristic Length ( $CL$ ) but far larger than the turbulence length scale—quantified hereafter as  $50 D_m c_\mu^{-1/4} k^{-1/2}$  (Sec. 4).

### 2.3. DG2-RANS- $k$ - $\varepsilon$ solver

With the DG2-RANS laminar flow solver, because Eq. (2) needs to be solved with  $D_m \neq 0$ , the components of the mean-flow viscous fluxes (in  $\mathbf{F}_{v_{\text{mean}}}$  and  $\mathbf{G}_{v_{\text{mean}}}$ ) are included, to involve second-order derivative terms, which must be integrated using a different local DG2 formulation that is suited for advective-diffusive PDEs.

With the DG2-RANS- $k$ - $\varepsilon$  turbulent flow solver, because Eq. (3) needs to be solved alongside Eq. (2) with  $k \neq 0$ ,  $\varepsilon \neq 0$  and  $D_t \neq 0$ , there are also: the other second-order derivative terms involved in the components of the turbulent-flow viscous fluxes (in  $\mathbf{F}_{v_{\text{turb}}}$  and  $\mathbf{G}_{v_{\text{turb}}}$ ); and, the two turbulent-flow variables (in  $\mathbf{U}_{\text{turb}}$ ) that must be stored/evolved using associated component-wise local spatial operators—including discretisations of the gradients of the turbulent-flow invicid and viscous flux components (in  $\mathbf{F}_{\text{turb}}$ ,  $\mathbf{G}_{\text{turb}}$ ,  $\mathbf{F}_{v_{\text{turb}}}$  and  $\mathbf{G}_{v_{\text{turb}}}$ ) and of the turbulent-flow source term components (in  $\mathbf{S}_{\text{turb}}$ ).

Therefore, the local DG2 formulation for advective-diffusive PDEs (Cockburn and Shu 1998) is used to devise the DG2-RANS- $k$ - $\varepsilon$  turbulent solver, to also include the DG2-RANS laminar flow solver. This DG2 formulation, is more complex, mathematically and numerically, than that of used in the DG2-SWE solver.

The added mathematical complexity stems from the need to reduce second-order derivative terms into first-order derivative terms (Miller et al. 2013). In doing so, the advective-diffusive  $5 \times 5$  RANS- $k$ - $\varepsilon$  system is, first, transformed into a  $13 \times 13$  system of advection-dominated PDEs (Sec. 2.3.1); and then solved by extending the advective DG2 formulation in Kesserwani et al. (2018), while adapting its existing wet-dry front treatments to preserve the positivity/stability for the mean-flow variables (Sec. 2.3.2). Numerically, the complexity arises from the further need to ensure positivity/stability-preserving turbulent-flow variables, which required adding a new combination of treatments for the turbulent-flow quantities (Sec. 2.3.3).

Computationally, the DG2-RANS- $k$ - $\varepsilon$  turbulent flow solver demands 39 cellwise degrees of freedom to store/evolve the local DG2 flow variable approximations (Sec. 2.3.2), and the DG2-RANS laminar flow solver needs 21 cellwise degrees of freedom, with both solvers needing a stricter  $\Delta t$ , than the DG2-SWE solver (Sec. 2.2), based on a  $Cr = 0.05$ .

In what follow, only the implementation of the DG2-RANS- $k$ - $\varepsilon$  turbulent flow solver is described as that of the DG2-RANS laminar flow solver is embedded within.

#### 2.3.1. Transformed $13 \times 13$ system

The second-order derivatives in the gradients of the mean-flow viscous flux components  $[(\partial F_{v_{\text{mean}_i}}/\partial x)_{i=1,2,3}]$  and  $(\partial G_{v_{\text{mean}_i}}/\partial y)_{i=1,2,3}$ , in Eq. (2)] and of the turbulent-flow viscous flux components  $[(\partial F_{v_{\text{turb}_i}}/\partial x)_{i=1,2}]$  and  $(\partial G_{v_{\text{turb}_i}}/\partial y)_{i=1,2}$ , in Eq. (3)] can be removed, by incorporating auxiliary variables to designate the first-order derivatives involved in Eqs. (2) and (3) (Hesthaven and Warburton 2007). Hence, the auxiliary variables:  $A_{u_x}, A_{u_y}, A_{v_x}, A_{v_y}, A_{k_x}, A_{k_y}, A_{\varepsilon_x}$  and  $A_{\varepsilon_y}$  are introduced based on the following identifies:

$$\begin{aligned} A_{u_x} &= \frac{\partial u}{\partial x} \text{ and } A_{u_y} = \frac{\partial u}{\partial y} \\ A_{v_x} &= \frac{\partial v}{\partial x} \text{ and } A_{v_y} = \frac{\partial v}{\partial y} \\ A_{k_x} &= \frac{\partial k}{\partial x} \text{ and } A_{k_y} = \frac{\partial k}{\partial y} \\ A_{\varepsilon_x} &= \frac{\partial \varepsilon}{\partial x} \text{ and } A_{\varepsilon_y} = \frac{\partial \varepsilon}{\partial y} \end{aligned} \quad (6)$$

Using Eq. (6) leads to new expressions for the mean-flow and turbulent-flow viscous flux components, further expressed in terms of the eight auxiliary variables, as shown in Eq. (7):

$$\begin{aligned} \mathbf{F}_{v_{\text{mean}}} &= (F_{v_{\text{mean}_i}})_{i=1,2,3}^T = \left[ 0, 2h(D_m + D_t)A_{u_x} - \frac{2}{3}hk, h(D_m + D_t)(A_{u_y} + A_{v_x}) \right]^T \\ \mathbf{G}_{v_{\text{mean}}} &= (G_{v_{\text{mean}_i}})_{i=1,2}^T = \left[ 0, h(D_m + D_t)(A_{u_y} + A_{v_x}), 2h(D_m + D_t)A_{v_y} - \frac{2}{3}hk \right]^T \\ \mathbf{F}_{v_{\text{turb}}} &= (F_{v_{\text{turb}_i}})_{i=1,2}^T = \left[ h\left(D_m + \frac{D_t}{\sigma_k}\right)A_{k_x}, h\left(D_m + \frac{D_t}{\sigma_\varepsilon}\right)A_{\varepsilon_x} \right]^T \\ \mathbf{G}_{v_{\text{turb}}} &= (G_{v_{\text{turb}_i}})_{i=1,2}^T = \left[ h\left(D_m + \frac{D_t}{\sigma_k}\right)A_{k_y}, h\left(D_m + \frac{D_t}{\sigma_\varepsilon}\right)A_{\varepsilon_y} \right]^T \end{aligned} \quad (7)$$

However, these eight auxiliary variables enlarge the  $5 \times 5$  advective-diffusive RANS- $k$ - $\varepsilon$  system into a  $13 \times 13$  system of advection-dominated PDEs that has: thirteen unknowns for the flow variable components, denoted by  $(W_j)_{j=1,2,\dots,13}$ ; and, thirteen equations, or spatial operators, denoted by  $(R_j)_{j=1,2,\dots,13}$ , as shown in Eq. (8):

$$\begin{aligned} \frac{\partial \mathbf{W}}{\partial t} &= \mathbf{R} \\ \mathbf{W} &= [(W_j)_{j=1,2,\dots,13}]^T = \left[ (U_{\text{mean}_i})_{i=1,2,3}, (U_{\text{turb}_i})_{i=1,2}, A_{u_x}, A_{u_y}, A_{v_x}, A_{v_y}, A_{k_x}, A_{k_y}, A_{\varepsilon_x}, A_{\varepsilon_y} \right]^T \\ \mathbf{R} &= [(R_j)_{j=1,2,\dots,13}]^T = \left[ (R_{\text{mean}_i})_{i=1,2,3}, (R_{\text{turb}_i})_{i=1,2}, (R_{\text{aux}_i})_{i=1,\dots,8} \right]^T \end{aligned} \quad (8)$$

$$\begin{aligned} R_{\text{mean}_i} &= -\frac{\partial F_{\text{mean}_i}}{\partial x} - \frac{\partial G_{\text{mean}_i}}{\partial y} + \frac{\partial F_{\text{mean}_i v_i}}{\partial x} + \frac{\partial G_{\text{mean}_i v_i}}{\partial y} + S_{\text{mean}_i} \\ R_{\text{turb}_i} &= -\frac{\partial F_{\text{turb}_i}}{\partial x} - \frac{\partial G_{\text{turb}_i}}{\partial y} + \frac{\partial F_{\text{turb}_i v_i}}{\partial x} + \frac{\partial G_{\text{turb}_i v_i}}{\partial y} + S_{\text{turb}_i} \\ (R_{\text{aux}_i})_{i=1,\dots,8} &= \left( \frac{\partial u}{\partial x}, \frac{\partial u}{\partial y}, \frac{\partial v}{\partial x}, \frac{\partial v}{\partial y}, \frac{\partial k}{\partial x}, \frac{\partial k}{\partial y}, \frac{\partial \varepsilon}{\partial x}, \frac{\partial \varepsilon}{\partial y} \right) \end{aligned}$$

In Eq.(8),  $\mathbf{W} = [(W_j)_{j=1,2,\dots,13}]^T$  is the vector packing the involved field variables, in the following order: the three components of the mean-flow variables  $(U_{\text{mean}_i})_{i=1,2,3}$ , the two components of the turbulent-flow variables  $(U_{\text{turb}_i})_{i=1,2}$  and the added auxiliary variables  $(A_{u_x}, A_{u_y}, A_{v_x}, A_{v_y}, A_{k_x}, A_{k_y}, A_{\varepsilon_x}, A_{\varepsilon_y})$ . On the right-hand side, vector  $\mathbf{R} = [(R_j)_{j=1,2,\dots,13}]^T$  includes the associated component-wise spatial operators, in the

following order:  $(R_{\text{mean}_i})_{i=1,2,3}$  adding the advective gradients,  $\partial Q/\partial x$  and  $\partial Q/\partial y$ , of the mean-flow inviscid flux components and of the mean-flow viscous flux components, and the mean-flow source term components,  $(S_{\text{mean}_i})_{i=1,2,3}$ , where  $Q = \{(F_{\text{mean}_i})_{i=1,2,3}, (G_{\text{mean}_i})_{i=1,2,3}, (F_{v_{\text{mean}_i}})_{i=1,2,3}, (G_{v_{\text{mean}_i}})_{i=1,2,3}\}$ ;  $(R_{\text{turb}_i})_{i=1,2}$  adding the advective gradients,  $\partial Q/\partial x$  and  $\partial Q/\partial y$ , of the turbulent-flow inviscid flux components and of the turbulent-flow viscous flux components, with  $Q = \{(F_{\text{turb}_i})_{i=1,2}, (G_{\text{turb}_i})_{i=1,2}, (F_{v_{\text{turb}_i}})_{i=1,2}, (G_{v_{\text{turb}_i}})_{i=1,2}\}$ ; and  $(R_{\text{aux}_i})_{i=1,\dots,8}$  including the advective gradients,  $\partial Q/\partial x$  and  $\partial Q/\partial y$ , of any of the auxiliary variables, with  $Q = \{u, v, k, \varepsilon\}$ .

Using the notations in Eq. (8), an extended advective DG2 formulation to that of Kesserwani et al. (2018) is presented (Sec. 2.3.2), with a new combination of stability/positivity-preserving treatments for the turbulent-flow quantities (Sec. 2.3.3). The present DG2 formulation uses a computational grid made of squared cells (i.e., a raster-formatted grid) and was coded in the LISFLOOD-FP hydraulic modelling environment for setting-up and running DG2-RANS- $k-\varepsilon$  turbulent flow simulations, or DG2-RANS laminar flow simulations using either the CPU or the GPU (Sec. 2.3.4).

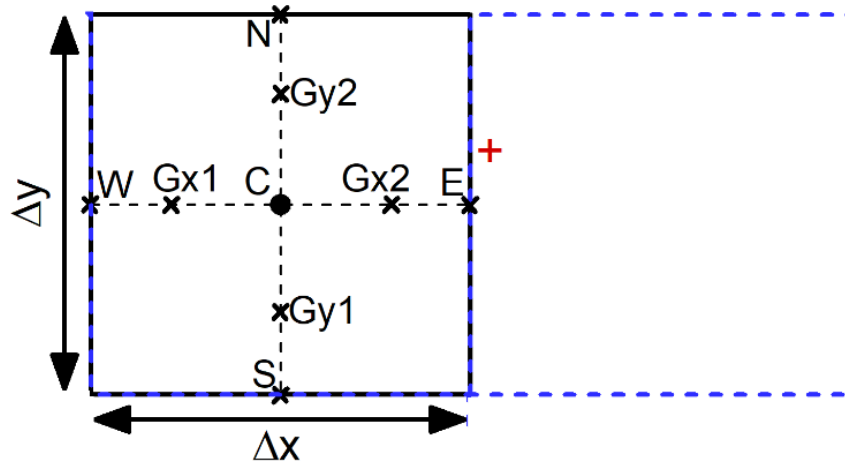


**Figure 1.** Stencil of a sample (local) cell used in the advective, slope-decoupled, DG2 formulation (Kesserwani et al. 2018). The sample cell is centred at point  $C$ , of squared dimensions ( $\Delta x = \Delta y$ ). Points  $N$ ,  $E$ ,  $S$  and  $W$  mark the northern, eastern, southern and western face centres that are shared with the four neighbouring cells – only eastern neighbouring cell is shown (in line with description provided in Appendix A); across these inter-cell points, numerical fluxes are evaluated based on linking the inner-limits (from the side of the sample cell) to the outer-limits (e.g., from the side of the neighbouring cell)–appended the “+” sign. Points  $Gx1$ ,  $Gx2$ ,  $Gy1$  and  $Gy2$  are inner-cell points for evaluating the source terms and physical fluxes (see also Appendix A).

### 2.3.2. Local DG2 approximation

Each component  $(W_j)_{j=1,2,\dots,13}$  is locally represented (cellwise) by a DG2 piecewise-planar approximation. For simplicity, this approximation is, hereafter, designated by  $W_j(x, y, t)$  for the sample cell shown in Fig. 1– centred at  $(x_C, y_C)$  and with equal cell dimensions ( $\Delta x = \Delta y$ ). The local DG2 piecewise-planar approximation

$W_j(x, y, t)$  is spanned by three degrees of freedom  $\{W_j^K(t)\}_{K=0,1x,1y}$ : where  $W_j^0(t)$  is an average coefficient, and  $W_j^{1x}(t)$  and  $W_j^{1y}(t)$  are  $x$ - and  $y$ -directional slope coefficients, to write as:

$$W_j(x, y, t) = \{W_j^K(t)\}_{K=0,1x,1y} = W_j^0(t) + 2\sqrt{3} W_j^{1x}(t) \left(\frac{x-x_c}{\Delta x}\right) + 2\sqrt{3} W_j^{1y}(t) \left(\frac{y-y_c}{\Delta y}\right) \quad (9)$$

The average and slope coefficients,  $W_j^K(t)$  in (Eq. 9) at any time  $t$ , need to be updated (for all the components,  $j = 1, 2, \dots, 13$ ), by one time-step  $\Delta t$ , to time  $t + \Delta t$ , using a two-stage Runge-Kutta explicit time integrator:

$$\begin{aligned} W_j^K(t + \Delta t/2) &= W_j^K(t) + \Delta t R_j^K \\ W_j^K(t + \Delta t) &= \frac{1}{2} [W_j^K(t) + W_j^K(t + \Delta t/2) + \Delta t R_j^K] \end{aligned} \quad (10)$$

In Eq. (10),  $R_j^K$  refers to any component-wise local spatial DG2 operator that needs to be evaluated from the coefficients  $W_j^K(t)$  during the first time-stage and, then similarly from coefficients  $W_j^K(t + \Delta t/2)$  to complete the second time-stage. It suffices, therefore, to describe the evaluation of  $R_j^K$  for the first time-stage. In doing so, evaluations for  $W_j(x, y, t)$  are required at the inner-cell points  $P = \{C, E, W, N, S, Gx1, Gx2, Gy1, Gy2\}$ , shown in Fig. 1, at which  $W_j(P, t)$  takes the following values, via Eq. (9):

$$\begin{aligned} W_j(E, t) &= W_j^0(t) + \sqrt{3}W_j^{1x}(t) & W_j(W, t) &= W_j^0(t) - \sqrt{3}W_j^{1x}(t) \\ W_j(N, t) &= W_j^0(t) + \sqrt{3}W_j^{1y}(t) & W_j(S, t) &= W_j^0(t) - \sqrt{3}W_j^{1y}(t) \\ W_j(Gx2, t) &= W_j^0(t) + W_j^{1x}(t) & W_j(Gx1, t) &= W_j^0(t) - W_j^{1x}(t) \\ W_j(Gy2, t) &= W_j^0(t) + W_j^{1y}(t) & W_j(Gy1, t) &= W_j^0(t) - W_j^{1y}(t) \\ W_j(C, t) &= W_j^0(t) & & \end{aligned} \quad (11)$$

These values are needed to, in turn, locally discretise the gradients of the advective flux components,  $(\partial Q/\partial x)_j^K$  and  $(\partial Q/\partial y)_j^K$ , and the source term components involved in the evaluation of the component-wise spatial DG2 operator  $R_j^K$ . In doing so, the evaluation of  $(\partial Q/\partial x)_j^K$  and  $(\partial Q/\partial y)_j^K$  is performed differently depending on whether  $Q \in I_{\text{inviscid}}$  or  $Q \in I_{\text{viscous}}$  (see Sec. A.1); where,  $I_{\text{inviscid}}$  includes all the inviscid flux components and  $I_{\text{viscous}}$  includes all the viscous flux the components (recall Sec. 2.3.1):

$$\begin{aligned} I_{\text{inviscid}} &= \{F_{\text{mean}1}, F_{\text{mean}2}, F_{\text{mean}3}, G_{\text{mean}1}, G_{\text{mean}2}, G_{\text{mean}3}, F_{\text{turb}1}, F_{\text{turb}2}, G_{\text{turb}1}, G_{\text{turb}2}\} \\ I_{\text{viscous}} &= \{F_{v_{\text{mean}1}}, F_{v_{\text{mean}2}}, F_{v_{\text{mean}3}}, G_{v_{\text{mean}1}}, G_{v_{\text{mean}2}}, G_{v_{\text{mean}3}}, F_{v_{\text{turb}1}}, F_{v_{\text{turb}2}}, G_{v_{\text{turb}1}}, G_{v_{\text{turb}2}}, u, v, k, \varepsilon\} \end{aligned} \quad (12)$$

In Appendix A, the evaluation of  $(\partial Q/\partial x)_j^K$  and  $(\partial Q/\partial y)_j^K$  is described (see Sec. A.1), building on the ‘‘slope-decoupled’’ advective DG2 formulation (Kesserwani et al. 2018), while including:

- External boundary conditions (subcritical) based on three user-specified choices: ‘‘Inflow’’, ‘‘Outflow’’ and ‘‘Closed’’ (as reported in Sec. A.1). These conditions are only activated at the wet cells located along any (of the four) boundary lines enclosing the (rectangular) computational domain.

- The ScWF, applied at near-dry-wall cells—the wet cells including at least one wet-dry front, or adjacent to dry cells (as reported in Sec. A.2). On the computational grid, the dry cells represent initial dry-wall areas and/or emerging areas of unsubmerged topographies. Therefore, such dry cells are identified, in the DG2-RANS- $k$ - $\varepsilon$  solver, every time-step; thereby, the near-dry-wall cells for applying the ScWF.
- The local (cellwise) DG2 evaluation of the mean-flow source term components,  $(S_{\text{mean}_i}^K)_{i=1,2,3}$ , and of the turbulent-flow source term components  $(S_{\text{turb}_i}^K)_{i=1,2}$  (as reported in Sec. A.3).

### 2.3.3. Stability/positivity-preserving treatments for the turbulent-flow quantities

In the local DG2 approximation of the turbulent-flow variables [i.e.,  $(U_{\text{turb}_i}^K)_{i=1,2}$  with  $K = 0, 1x, 1y$ ],  $k$  and  $\varepsilon$  are expected to take small positive values, usually at a scale less than  $10^{-2}$ , at all the wet cells throughout a simulation. However, spurious noises may still develop causing negative  $k$  or  $\varepsilon$  values that lead to instabilities. Such noises could arise from the combined effect of roundoff errors, the wet-dry front treatments, and the local limiting of slope coefficients (involved in the local DG2 approximations). Therefore, the following additional numerical treatments for the turbulent-flow quantities were found necessary to ensure overall reliability:

- **Elimination of roundoff errors.** Double-precision computations are utilised to minimise roundoff errors, thus assuming a roundoff error around  $\pm 10^{-14}$ . Because of this, zero values for  $k$  and  $\varepsilon$  should not be allowed in the local DG2 approximation of  $(U_{\text{turb}_i})_{i=1,2}$  to avoid them taking smaller magnitudes than roundoff error. Therefore, the smallest value that either of  $k$  and  $\varepsilon$  could take in  $(U_{\text{turb}_i}^K)_{i=1,2}$  was set to the tolerance,  $k_{\text{tol}} = \varepsilon_{\text{tol}} = 10^{-12}$ , starting from the initial conditions of the average coefficients,  $k^0 = k_{\text{tol}}$  and  $\varepsilon^0 = \varepsilon_{\text{tol}}$ , with zero slope coefficients ( $k^{1x}=k^{1y}=0$  and  $\varepsilon^{1x}=\varepsilon^{1y}=0$ ). This tolerance, although larger than the magnitude of the roundoff error, is still small enough to ensure overall reliable predictions – also because using it leads to local DG2 evaluation of  $D_t$  that is below  $10^{-12}$  (i.e., remaining significantly lower than  $D_m = 10^{-6}$ ).
- **Adaptation of the wet-dry front treatments.** The wet-dry front treatments (Kesserwani et al., 2018; Shaw et al., 2021)—incorporated in the local DG2 approximation of  $(U_{\text{mean}_i})_{i=1,2,3}$ —must also be adapted to the velocities involved in the local DG2 approximation of  $(U_{\text{turb}_i})_{i=1,2}$ . Moreover, following Cea et al. (2007), the adaptation considers avoiding zero values for the average coefficients  $k^0$  and  $\varepsilon^0$  at the dry cells, assigning them as  $k^0 = k_{\text{tol}}$  and  $\varepsilon^0 = \varepsilon_{\text{tol}}$ , with zero slope coefficients ( $k^{1x}=k^{1y}=0$  and  $\varepsilon^{1x}=\varepsilon^{1y}=0$ ).

• **Positivity-preserving local slope limiting.** The localisation procedure (Krivodonova et al. 2004) including the *generalised minmod limiter* (Cockburn and Shu 2001) is applied to locally limit the variation of the slope coefficients  $(U_{\text{turb}_i}^{1x})_{i=1,2}$  and  $(U_{\text{turb}_i}^{1y})_{i=1,2}$ —as with  $(U_{\text{mean}_i}^{1x})_{i=1,2,3}$  and  $(U_{\text{mean}_i}^{1y})_{i=1,2,3}$  (Ayog et al. 2021). This localisation procedure restricts the activation of the *generalised minmod limiter* to only the wet cells where potentially strong discontinuities could develop, thereby damping spurious oscillations from arising in  $(U_{\text{mean}_i}^{1x,1y})_{i=1,2,3}$ . However, it can still overlook smaller-scale oscillations that could still impact the  $k$  or  $\varepsilon$  variables [in  $(U_{\text{turb}_i}^{1x,1y})_{i=1,2}$ ]. To remove potentially remaining smaller-scale oscillations, the positivity reconstruction technique of Bonev et al. (2018) was incorporated to further refine local slope-limiting for the  $k$  or  $\varepsilon$  variables before evaluating the discrete DG2 spatial operators. For the variable  $k$ , for example, the positivity reconstruction initially imposes  $k^0 = k_{\text{tol}}$  if  $k^0 \leq k_{\text{tol}}$  with  $k^{1x} = k^{1y} = 0$ , or otherwise ( $k^0 > k_{\text{tol}}$ ), retains the  $k^0$  value, but potentially rescales slope coefficients  $k^{1x}$  and  $k^{1y}$  via the following indicators:

$$\begin{aligned}\theta_x &= \min\left(1, \frac{k^0}{k^0 - \min(k_E, k_W)}\right) \\ \theta_y &= \min\left(1, \frac{k^0}{k^0 - \min(k_N, k_S)}\right)\end{aligned}\tag{13}$$

In Eq. (13), both indicators  $\theta_x$  and  $\theta_y$  take the value of 1 when the evaluated local DG2 approximation of  $k$  takes positive values at all points  $P$  inside the sample cell (Fig. 1). Otherwise, if one of the indicators  $\theta_x$  or  $\theta_y$  is below 1, the following rescaling must be applied for the slope coefficients,  $k^{1x}$  and  $k^{1y}$ , for stability:

$$\begin{aligned}k^{1x} &= \begin{cases} -\left(\frac{k^0 - k_{\text{tol}}}{\sqrt{3}}\right) & \text{if } \theta_x < 1 \text{ and } k_W > k_E \\ \left(\frac{k^0 - k_{\text{tol}}}{\sqrt{3}}\right) & \text{if } \theta_x < 1 \text{ and } k_E > k_W \end{cases} \\ k^{1y} &= \begin{cases} -\left(\frac{k^0 - k_{\text{tol}}}{\sqrt{3}}\right) & \text{if } \theta_y < 1 \text{ and } k_S > k_N \\ \left(\frac{k^0 - k_{\text{tol}}}{\sqrt{3}}\right) & \text{if } \theta_y < 1 \text{ and } k_N > k_S \end{cases}\end{aligned}\tag{14}$$

• **Time-stepping criterion.** The time-step  $\Delta t$  is the minimum allowable one across all the computational cells to ensure stability. It is calculated based on the Courant–Friedrichs–Lewy condition, with a Courant number  $Cr$  of 0.05 to ensure stability for the invicid, viscous and turbulent-eddy terms. After each update, Eq. (10), the time-step  $\Delta t$  is calculated as follows:

$$\Delta t = Cr \times \min \left[ \frac{\Delta x}{|u_c| + \sqrt{gh_c}}, \frac{\Delta y}{|v_c| + \sqrt{gh_c}}, \frac{\Delta x \Delta x}{D_m + (D_t)_c}, \frac{\Delta y \Delta y}{D_m + (D_t)_c} \right] \quad (15)$$

#### 2.3.4. Open-source integration, parallelisation and reproducibility

The code, of the DG2-RANS- $k-\varepsilon$  turbulent flow solver, was programmed and integrated into the LISFLOOD-FP modelling environment (Shaw et al. 2021), building upon the two existing DG2-SWE solver's codebases (Shaw et al. 2021): the OpenMP version, for making DG2-RANS- $k-\varepsilon$  simulations on a multi-core CPU; and the CUDA version for faster DG2-RANS- $k-\varepsilon$  simulations on the GPU. The code of DG2-RANS- $k-\varepsilon$  turbulent flow solver is open source on Zenodo under a GPLv3.0 (Hajihassanpour et al. 2024).

In the Zenodo repository (Hajihassanpour et al. 2024), the (test-specific, Sec. 4) setup initial condition files (to start simulations)–DG2 approximation (raster) data of both the initial flow variables and ground elevations (Sec. 3.1)–are also included to reproduce the simulated test cases (Sec. 4). In addition to the initial conditions, the LISFLOOD-FP code needs initial parametrisations (e.g., to select among the DG2-RANS- $k-\varepsilon$  turbulent flow solver and the DG2-RANS laminar flow solver, or whether to run on the CPU or the GPU), which are documented in a dedicated webpage at [https://www.seamlesswave.com/DG2\\_RANS](https://www.seamlesswave.com/DG2_RANS).

**Table 1.** Test cases (subcritical flow, developing vortical structures past topographies) used to evaluate the DG2-RANS- $k-\varepsilon$  turbulent flow solver (Sec. 4.1) and DG2-RANS laminar flow solver (Sec. 4.2), contrasted against DG2-SWE solver; the test-specific Reynolds number ( $Re$ ), Characteristic Length ( $CL$ ) and Aspect Ratio ( $AR$ ).

Evaluation test cases (Sec. No.)	$Re$	$CL$ (m)	$AR^*$
Turbulent flows (4.1)			
Vortex shedding past a conical island (4.1.1)–submerged	6k	0.054 (surface-water level)	28.1
Vortex shedding past a conical island (4.1.1)–surface-piercing	5k	0.045 (surface-water level)	
Recirculation flow in sharp building cavities (4.1.2)	112k	0.35 (width of building cavities)	51.1
Flow past a square block in a diverting T-junction (4.1.3)	7.4k	0.05 (square block dimension)	6.52
Laminar flows (4.2)			
Wake past a cylinder (4.2.1)	0.2k	0.004 (diameter of cylinder)	0.85
Wake interactions past many cylinders (4.2.2)	0.22k		2.0

\* The  $AR$  of a channel's width to the flow depth (Shinnee et al. 2021) can be used to measure the validity of the inviscid SWE assumption: the bigger the  $AR$ , the more significant the influence of the size and strength of vortical flow structures; thus, the less competitive would the DG2-SWE solver be usable as an alternative to the DG2-RANS- $k-\varepsilon$  solver.

### 3. Evaluation approach and runtimes

DG2-RANS/DG2-RANS- $k-\varepsilon$  and DG2-SWE simulations were run to reproduce five test cases (summarised in Table 1), all developing quasi-steady vortical flow structures that occur past (un)submerged topographies. The first three turbulent flow test cases involve compound eddies of different sizes, that could only be reproduced by the DG2-RANS- $k-\varepsilon$  solver from the medium resolution (Table 2, Sec. 4.1). The last two laminar flow test cases involve wakes that are more reliably reproduced by the DG2-RANS solver from the medium resolution

(Table 2, Sec. 4.2). In contrast, the DG2-SWE simulations provide the most reliable predictions for the coarse resolution, at which it tends to become usable as an implicit large eddy simulator (Table 2, Sec. 4).

### 3.1. Integration of the topographies and robustness

DG2 approximation data of ground elevations [i.e., three raster data files, defining the degrees of freedoms for spanning the (time-invariant) ground elevation  $z$ —described in Shaw et al. (2021)’s Sec. 2.1.1], were generated from a (test-specific) raster-formatted Digital Elevation Model (DEM). The DEMs were created such that dry-wall areas, located inside the computational domain, are given an unrealistically high ground elevation value [e.g., areas spanning: the rectangular blocks in-between cavities (Sec. 4.1.2), the main-branch’s square block and the rectangular walls in the side-branch (Sec. 4.1.3)]. Therefore, based on the setup initial condition files—DG2 approximation data of initial flow variables and ground elevations— the in-domain areas of unsubmerged topographies will be identified as dry cells at the start of any simulation. However, the identification of dry cells is performed every time-step during simulations.

Videos to watch the performance of the DG2-RANS- $k-\epsilon$  turbulent flow solver for most of the simulated test cases are available on: [https://www.seamlesswave.com/DG2\\_RANS](https://www.seamlesswave.com/DG2_RANS) (videos linked to test-case images). The animated simulation of “Vortex shedding past a conical island (4.1.1)—surface-piercing” demonstrates the solver’s ability to deal with moving dry-wall boundaries arising from continuously-and-periodically-moving wet-dry fronts. Whereas the animated simulation of the “Flow past a square block in a diverting T-junction (4.1.3)” demonstrates robustness: the DG2-RANS- $k-\epsilon$  turbulent flow solver successfully converged despite starting the simulation from zero initial flow variables.

### 3.2. Simulation set-up and resolutions

The DG2-RANS/DG2-RANS- $k-\epsilon$  simulations used the “Inflow” and “Outflow” boundary conditions along the computational domain’s inflow and outflow, respectively, or otherwise the “Closed” boundary conditions were used. Similar boundary conditions were used with the DG2-SWE simulations. The simulations are explored for three resolutions coarse, medium and fine—the coarse being strictly smaller than the  $CL$  and the fine being as close as possible to the turbulence length scale (depending on the specifics of each test case, Sec. 4).

The selected resolutions led to small-sized computational grids (20k-to-250k cells, Table 2), on which DG2-SWE simulations yield similar CPU (10 threads) and GPU runtimes (V100 card)—demonstrated in Shaw et al. (2021). Therefore, only the GPU runtimes are reported for the DG2-SWE simulations (Table 2). Whereas

the DG2-RANS/DG2-RANS- $k-\epsilon$  simulation runtimes are reported for both the CPU and the GPU runs (Table 2), with analysis of GPU-to-CPU speedups and of GPU speedups with respect to the DG2-SWE simulations.

**Table 2.** CPU and GPU runtimes for the DG2-RANS- $k-\epsilon$  turbulent flow simulations (Sec. 4.1) and the DG2-RANS laminar flow simulations (Sec. 4.2); GPU runtimes for the DG2-SWE simulations—at fine, medium and coarse resolutions.

Test case (Sec. No.)	DG2-RANS- $k-\epsilon$ solver						DG2-SWE solver		
	CPU runtime (hr) [cells No. (in k)]			GPU runtime (hr) [CPU/GPU]			GPU runtime (hr) [RANS- $k-\epsilon$ /SWE]		
Turbulent flows (4.1)	Coarse	Medium	Fine	Coarse	Medium	Fine	Coarse	Medium	Fine
Vortex shedding past a conical island (4.1.1)–submerged	1.1 [16.4]	12.3 [64.9]	102.1 [259.7]	0.75 [1.46]	2.9 [4.2]	17.75 [5.75]	0.03 [25]	0.08 [36.3]	0.3 [59.2]
Recirculation flow in sharp building cavities (4.1.2)	--	6.21 [21.0]	38.5 [84.0]	--	2.7 [2.3]	8.3 [4.63]	--	0.04 [67.5]	0.1 [83]
Flow past a square block in a diverting T-junction (4.1.3)	2.2 [35.5]	14.5 [142.1]	218.5 [568.0]	0.83 [2.65]	4.66 [3.11]	34.5 [6.33]	0.03 [27.7]	0.1 [46.6]	0.38 [90.8]
Laminar flows (4.2)	DG2-RANS solver						DG2-SWE solver		
	CPU runtime (hr) [cells No. (in k)]			GPU runtime (hr) [CPU/GPU]			GPU runtime (hr) [RANS/SWE]		
Wake past a cylinder (4.2.1)	Coarse	Medium	Fine	Coarse	Medium	Fine	Coarse	Medium	Fine
Wake past a cylinder (4.2.1)	9.6 [15.6]	72.2 [62.4]	617.8 [249.8]	9.0 [1.06]	32.0 [2.25]	200.0 [3.09]	0.18 [50]	--	--
Wake interactions past many cylinders (4.2.2)	--	1309.1 [1000]	--	--	199.3 [6.56]	--	2.5 [--]	--	--

### 3.3. Runtime cost

The computational cost of the DG2-RANS/DG2-RANS- $k-\epsilon$  solver is greatly higher than that of the DG2-SWE solver since (Secs. 2.2 and 2.3): (i) in the former, there are 12 to 30 additional degrees of freedom involved, adding to the 9 degrees of freedom involved in the latter, resulting in larger (cellwise) operational costs; (ii) the former must at least use the medium resolution to acquire reliable simulations, whereas only the coarse resolution is suited for the latter to acquire acceptable simulations (shown in Sec. 4); and, (iii) the former has a greatly smaller time-step than that of the latter. Consequently, as shown in Table 2, the former entails greatly larger runtimes (hours to days) than the latter (minutes to hours) in all the simulated test cases.

In Table 2, the runtimes by the DG2-RANS/DG2-RANS- $k-\epsilon$  simulations are shown for both the CPU and the GPU runs, including the relative GPU-to-CPU speedup ratios. Also, the GPU runtimes from the DG2-SWE simulations are included with the associated speedup ratios with respect to the DG2-RANS/DG2-RANS- $k-\epsilon$  simulations. On average, the runtimes of the DG2-RANS/DG2-RANS- $k-\epsilon$  solver are reduced, by around 7-fold, when doubling the resolution from fine to medium and further reduced, by around 2-to-6-fold, when running on the GPU. Notably, the DG2-RANS/DG2-RANS- $k-\epsilon$  solver achieve considerable speedups on the

GPU despite using small-sized grids (e.g., 20k-to-250k cells, Table 2), indicating that the use of GPU is suited to alleviate the costs of storing/evolving its large number of degrees of freedom.

Compared to the DG2-SWE solver, the DG2-RANS/DG2-RANS- $k-\epsilon$  solver is 25-to-90-fold slower to run. However, the DG2-SWE solver's costs are incomparable with the DG2-RANS/DG2-RANS- $k-\epsilon$  solver's costs: the former tends to succeed (as an implicit large eddy simulator) for the coarse resolution; whereas, the latter can succeed from the medium resolution (Table 2, Sec. 4). Overall, the analysis of runtime costs suggests using medium-resolution DG2-RANS/DG2-RANS- $k-\epsilon$  GPU runs in favour of efficiency to fairly match the accuracy of the fine-resolution runs (as shown in the results and discussion, Sec. 4).

### 3.4. Quantitative comparison metrics

The simulated velocity fields will be compared qualitatively and quantitatively (Sec. 4). The quantitative metrics will be based on three scores, hereafter denoted by:  $L^1$ ,  $R^2$  and  $RI$  and shown in Eqs. (16-18). For any simulated velocity field, these scores were evaluated with reference to measured data (limited and test-specific); and, more generally, with reference to the most accurate simulation data (i.e., the fine-resolution DG2-RANS/DG2-RANS- $k-\epsilon$  simulation available at all grid points) when comparing two simulated 2D spatial maps.

The  $L^1$  score, or  $L^1$ -norm error in (Eq. 16), measures the average deviation between the simulated and the reference data ( $L^1$  closer to 0 means less deviation); the  $R^2$  score, or the coefficient of determination (square of the correlation coefficient, Eq. 17) measures the extent to which the simulated data fits the reference data (the closer the  $R^2$  to 1 the better the fit); and the  $RI$  score, or the relevance index (Eq. 18), measures directional alignments between the simulated and reference data [ $RI = 1$  (perfect alignment) and -1 (opposite alignment)].

$$L^1 = \frac{1}{N_s} (\sum_{p=1}^{N_s} |v_p^{\text{Ref}} - v_p^{\text{Sim}}|) \quad (16)$$

$$R^2 = \left\{ \frac{\sum_{p=1}^{N_s} [(v_p^{\text{Ref}} - \bar{v}_p^{\text{Ref}})(v_p^{\text{Sim}} - \bar{v}_p^{\text{Sim}})]}{\sqrt{[\sum_{i=p}^{N_s} (v_p^{\text{Ref}} - \bar{v}_p^{\text{Ref}})^2][\sum_{p=1}^{N_s} (v_p^{\text{Sim}} - \bar{v}_p^{\text{Sim}})^2]}} \right\}^2 \quad (17)$$

$$RI = \frac{1}{N_s} \left\{ \sum_{p=1}^{N_s} \left[ \frac{(u_p^{\text{Ref}} u_p^{\text{Sim}} + v_p^{\text{Ref}} v_p^{\text{Sim}})}{V_p^{\text{Ref}} V_p^{\text{Sim}}} \right] \right\} \quad (18)$$

In Eqs. (16-18),  $N_s$  is the total number of points considered in the velocity data sample; superscripts ‘‘Ref’’ vs. ‘‘Sim’’ designate reference vs. simulated data, respectively;  $u_p$ , and  $v_p$  are the longitudinal and transverse velocity components at any sample points  $p$ , respectively; and  $V_p = (u_p^2 + v_p^2)^{0.5}$  is the velocity magnitude.

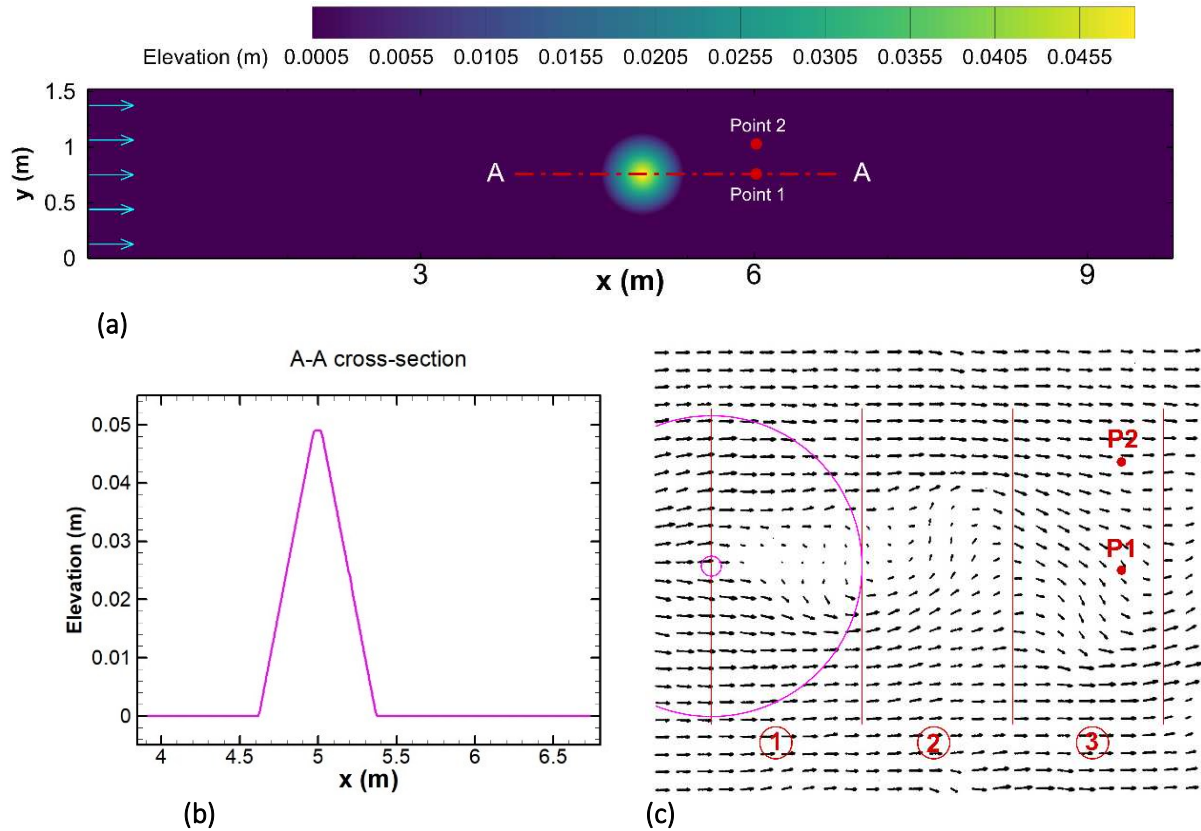


Figure 2. Vortex shedding past a conical island: (a) domain area showing the steady inflow (using arrows) and the conical island; (b) the profile of the conical island along section A-A; and (c) observed, instantaneous, velocity field [reprinted from Lloyd and Stansby (1997a) with permission from ASCE] in the wake region.

## 4. Results and discussion

### 4.1. Turbulent flows

#### 4.1.1. Vortex shedding past a conical island

A turbulent flow ( $Re = 6,210$ ) with periodic vortex shedding past an island is investigated (Lloyd and Stansby 1997a). The domain area is 9.75 m long and 1.52 m wide; it has a flat and smooth bed ( $n_M = 0.014$ ) including a conical island located 5 m from the inflow (Fig. 2a). The height of the conical island is 0.049 m, its side slope is  $8.0^\circ$ , and its top and bottom base diameters are 0.05 and 0.75 m, respectively (Fig. 2b). The inflow (along the transverse cross-section  $x = 0$  m) has a velocity, of  $U_\infty = 0.115 \text{ s}^{-1} \text{ m}$ , and the surface-water level is 0.054 m ( $CL = 0.054$  m, Table 1), slightly submerging the island past which the quasi-steady flow involves periodic vortex shedding cycles. In Fig. 2c, an observed instantaneous velocity field in the wake region past the island [from  $x = 5$  m (centre of the island) to 6.2 m past the two-gauge points P1 (6.02 m, 0.76 m) and P2 (6.02 m, 1.03 m)] is shown (Lloyd and Stansby 1997a), which is divided into equidistant subregions of 0.75 m (following: [http://coastal.usc.edu/currents\\_workshop/problems/prob1.html](http://coastal.usc.edu/currents_workshop/problems/prob1.html)). Along the area of vortex shedding ( $0.6 \text{ m} \leq y \leq 0.9 \text{ m}$  and  $5 \text{ m} \leq x \leq 6.2 \text{ m}$ ) subregion 1 exhibits a zone of recirculating flow and subregions 2 and 3 are

dominated by flows that are skewed towards P2 and P1, respectively. Outside this area, the flow is quite rectilinear (Fig. 2c). At P1 and P2, the measured time-series of  $v$ -velocity components allow the number of vortex-shedding period cycles ( $N_{cyc}$ ) to be calculated, indicating roughly that  $N_{cyc} = 8$  for around 80 s (i.e., based on the plots of  $v$ -velocity time-series in [http://coastal.usc.edu/currents\\_workshop/problems/prob1.html](http://coastal.usc.edu/currents_workshop/problems/prob1.html)).

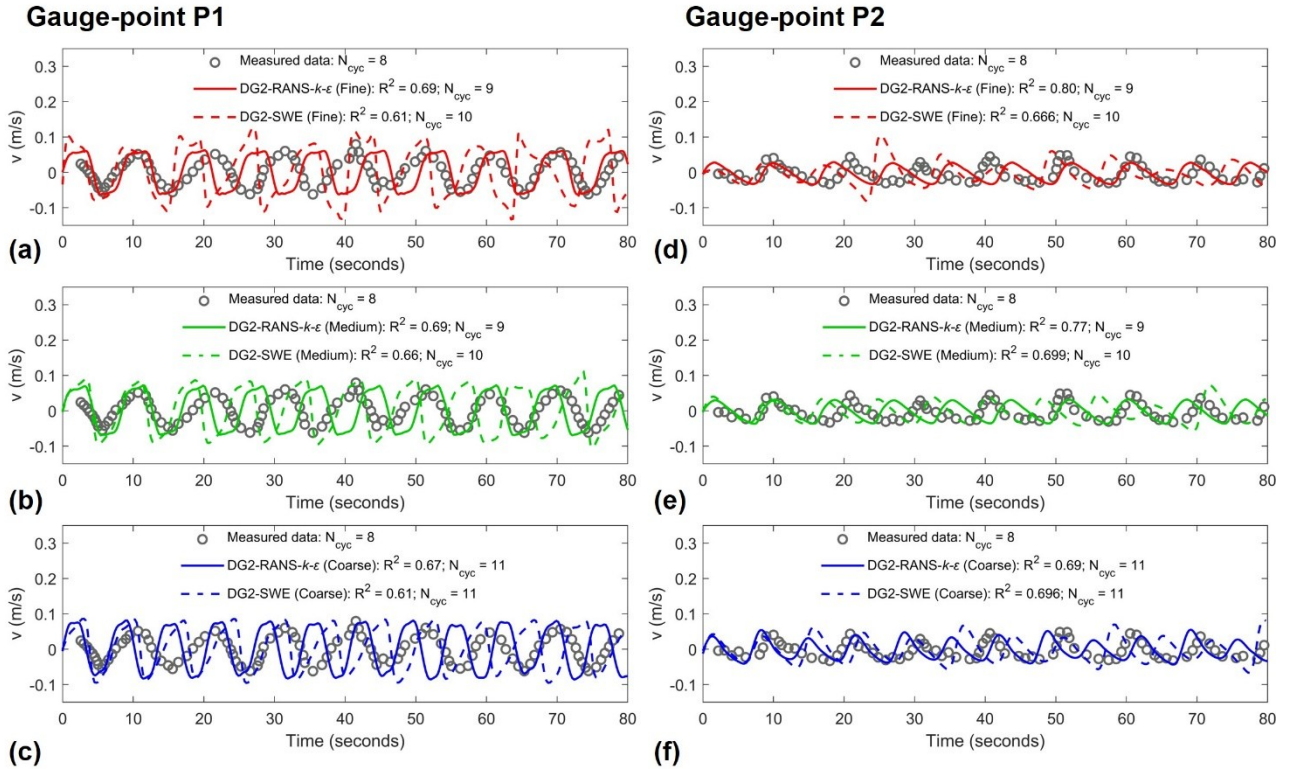


**Figure 3.** Vortex shedding past a conical island. Time-series of simulated transverse velocity profiles compared with the measured data (Lloyd and Stansby 1997): (a)-(c) at gauge-point P1 from the fine-, medium-, and coarse-resolution DG2-RANS- $k$ - $\epsilon$  and DG2-SWE simulations; and (d)-(f) at gauge-point P2 for the same simulations, respectively. The  $R^2$  scores shown were calculated with reference to the measured data and  $N_{cyc}$  represents the number of period cycles per data.

Fine- (0.0076 m or 0.14 $CL$ , using 259,772 cells), medium- (0.0152 m or 0.28 $CL$ , using 64,943 cells), and coarse-resolution (0.0304 m or 0.56 $CL$ , using 16,422 cells) DG2-RANS- $k$ - $\epsilon$  and DG2-SWE simulations were run, such that the medium resolution matches that reported in Lloyd and Stansby (1997a). The simulation time was 500 s and the time-series of  $v$ -velocity profiles were extracted during that last 80 s (between 420 and 500 s) to be compared with the measured  $v$ -velocity time-series, of relevance to assess the ability of the DG2-RANS- $k$ - $\epsilon$  and DG2-SWE solvers in tracking vortex-shedding period cycles. A video of the fine-resolution DG2-RANS- $k$ - $\epsilon$  simulation is on [https://www.seamlesswave.com/DG2\\_RANS](https://www.seamlesswave.com/DG2_RANS) (linked to the test-case image).

In Fig. 3, the simulated  $v$ -velocity time-series are plotted and compared with the measured data at P1 (along section A-A) and at P2 (along the rectilinear flow), shown in Fig. 3a-3c and Fig. 3d-3f, respectively. With the DG2-RANS- $k$ - $\epsilon$  simulations, the tracking of the vortex-shedding period cycles is most accurately achieved at the fine-resolution (highest  $R^2$  scores, all calculated with respect to the measured data)—as expected,

since 0.0076 m is close to the turbulence length scale (0.007 m). This accurate tracking is acceptably preserved at the medium resolution (slightly lower  $R^2$  scores), that leads to the same number of vortex-shedding period cycles as at the fine resolution:  $N_{cyc} = 9$ , which is the closest to  $N_{cyc} = 8$  seen in the measured data. In contrast, at the coarse resolution, a larger  $N_{cyc} = 11$  is predicted, revealing the inability of the DG2-RANS- $k-\epsilon$  solver to track the vortex-shedding period cycles below the medium resolution.

With the DG2-SWE simulations (also shown in Fig. 3a-3c and Fig. 3d-3f), the tracking ability of the number of vortex-shedding period cycles is at best similar to that of the coarse-resolution DG2-RANS- $k-\epsilon$  simulation (better-to-similar  $R^2$  scores). At both the fine and medium resolution,  $N_{cyc} = 10$  is predicted but with an enlarged velocity magnitude compared that seen in the DG2-RANS- $k-\epsilon$  simulations and the measured data; whereas, at the coarse resolution, the velocity magnitude is fairly reproduced but with a larger  $N_{cyc} = 11$ . Hence, none of the DG2-SWE simulations can compete with the medium- and fine-resolution DG2-RANS- $k-\epsilon$  simulations when reproducing the vortex-shedding period cycles and the velocity magnitude. Next in Fig. 4, the simulated 2D spatial maps of velocity fields were plotted at the first half-period cycle [i.e., based on the  $v$ -velocity profiles at P1, around 5 s (Fig. 3a-3c)]. However, any score shown in Fig. 4 (for  $L^1$ ,  $R^2$  and  $RI$ ) is an average of the scores calculated from the (unshown) simulated 2D spatial maps at all the cycles.

In Fig. 4, the instantaneous velocity fields in the wake region (Fig. 2c) are shown in terms of direction and magnitude for the coarse-, medium- and fine-resolution DG2-SWE and DG2-RANS- $k-\epsilon$  simulations. Except for the dead zone of flow recirculation in subregion 1, all the simulations predict the same directional flow alignment in subregions 2 and 3. In these regions, the velocity magnitude is consistently similar for the DG2-RANS- $k-\epsilon$  simulations but significantly deviates for the DG2-SWE simulations, which exhibit spurious overestimations that tend to amplify with the resolution refinement. In subregion 1, only the medium- and fine-resolution DG2-RANS- $k-\epsilon$  simulations could well reproduce the patterns of the dead zone of flow recirculation detected in the observed velocity field (Fig. 2c); whereas a spuriously transverse flow occurs with the coarse-resolution DG2-RANS- $k-\epsilon$  simulation that is further amplified with the DG2-SWE simulations.

Because a score shown in Fig. 4 (among the  $L^1$ ,  $R^2$  and  $RI$  scores) is the average of the scores extracted from instantaneous velocity fields at all the vortex-shedding period cycles, the standard deviation was also calculated to analyse the consistency in the spatial predictions across the period cycles. The average scores for the medium-resolution DG2-RANS- $k-\epsilon$  simulation (i.e.,  $L^1 = 0.003$ ,  $R^2 = 0.98$  and  $RI = 0.99$ ) show that it is very close to the fine-resolution simulation, which is relatively not the case for the coarse-resolution simulation

(i.e.,  $L^1 = 0.011$ ,  $R^2 = 0.86$  and  $RI = 0.93$ ), reinforcing the need to use at least the medium resolution. Moreover, the standard deviation is found zero with the DG2-RANS- $k-\epsilon$  simulations despite the resolution, which signals that the same spatial predictions occurred at any period cycle.

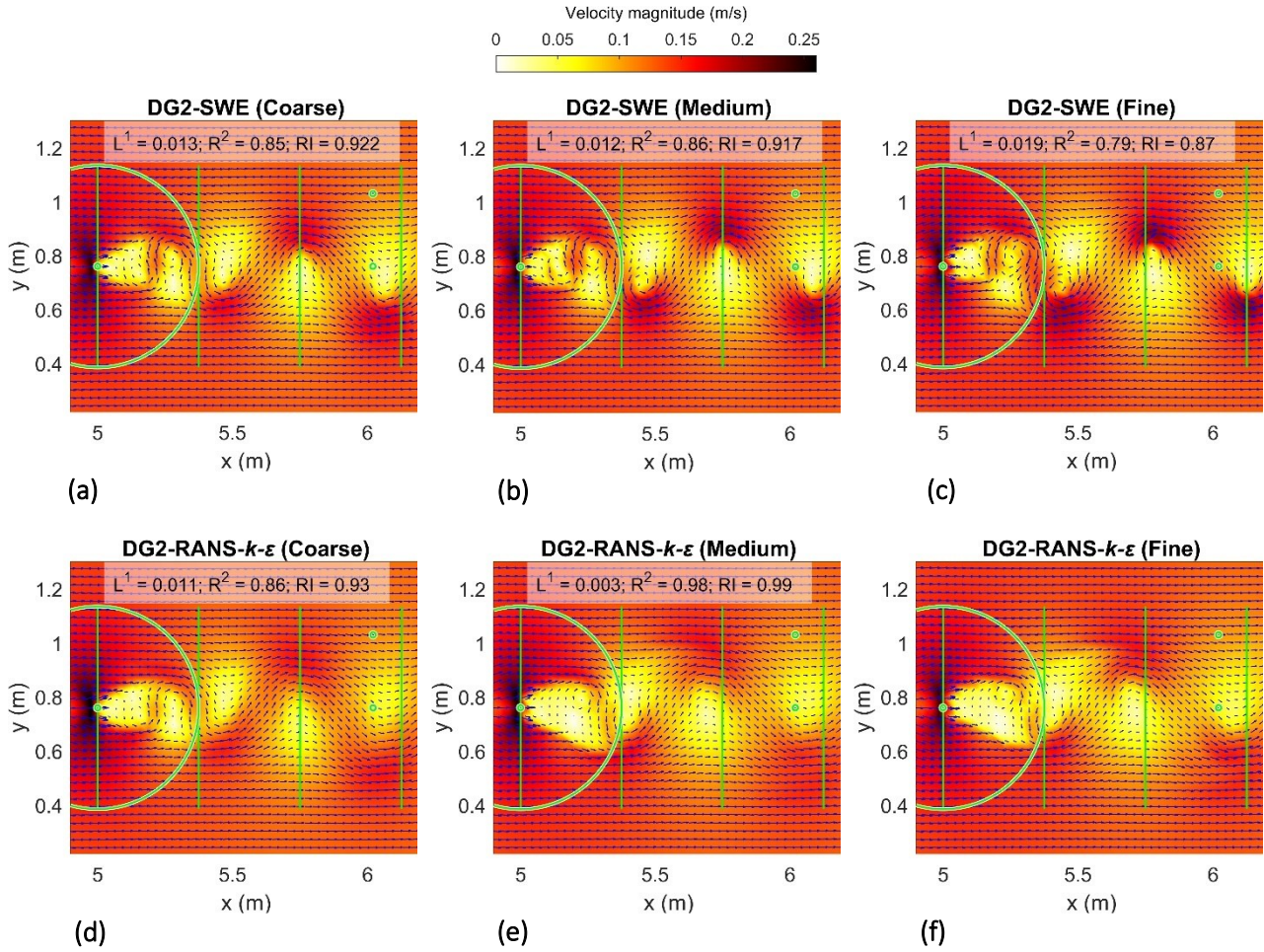


**Figure 4.** Vortex shedding past a conical island: (a-c) and (d-f) show the instantaneous (i.e., at around 5 s in Fig. 3a-3c, first half-period cycle) 2D map of velocity field and magnitude from the coarse-, medium- and fine-resolution DG2-SWE and DG2-RANS- $k-\epsilon$  simulations, respectively; any score for  $L^1$ ,  $R^2$  and  $RI$  was time-averaged from the scores (i.e., with reference to the simulation data shown in sub-figure 4f) calculated for all the 2D maps at the period cycles.

With the DG2-SWE simulations, the averages (scores shown in Fig. 4) and standard deviations are found to be the largest with fine resolution (i.e.,  $L^1 = 0.019 \pm 0.007$ ,  $R^2 = 0.79 \pm 0.05$  and  $RI = 0.87 \pm 0.089$ ), but reduced with the medium resolution (i.e.,  $L^1 = 0.012 \pm 0.002$ ,  $R^2 = 0.86 \pm 0.02$  and  $RI = 0.917 \pm 0.025$ ), and reduced further with the coarse resolution (i.e.,  $L^1 = 0.013 \pm 0.001$ ,  $R^2 = 0.85 \pm 0.01$  and  $RI = 0.922 \pm 0.010$ ). This reinforces that the DG2-SWE simulation at the coarse resolution is able to provide more reliable and consistent prediction of time-averaged spatial velocity fields than at the finer resolutions.

For the same island, the surface-piercing case (Lloyd and Stansby 1997b) was also simulated, starting from a surface-water level of 0.045 m ( $CL = 0.045$  m, Table 1). As there is no velocity time-series reported for this case, its DG2-RANS- $k-\epsilon$  simulation was not analysed. However, a video showing the medium-resolution

DG2-RANS- $k-\varepsilon$  simulation is on [https://www.seamlesswave.com/DG2\\_RANS](https://www.seamlesswave.com/DG2_RANS) (linked to the test-case image). As shown in the video, the DG2-RANS- $k-\varepsilon$  solver can reproduce periodic vortex-shedding, matching that seen for a measured instantaneous velocity vector field at the same resolution [i.e., Fig. 6(a) in Lloyd and Stansby (1997b), which is shown in the test-case image on [https://www.seamlesswave.com/DG2\\_RANS](https://www.seamlesswave.com/DG2_RANS)].

#### 4.1.2. Recirculation flow in sharp building cavities

A turbulent flow ( $Re = 112,673$ ) is considered in a computational domain including steep (dry) buildings (i.e., grey rectangles in Fig. 5a, assigned a high ground elevation), that are 0.35 m wide ( $CL = 0.35$  m, Table 1), defining side-wall “sharp building cavities”. Experiments (Rubinato 2015), made at the University of Sheffield ( $n_M = 0.011$ , longitudinal bed-slope is  $0.001 \text{ m m}^{-1}$ ), included instantaneous velocity fields from particle image velocimetry (PIV) measurements at 16 cm resolution (Rubinato et al. 2021). The inflow is not rectilinear along the transverse cross-section (i.e., blue arrows in Fig. 5a), and was extracted, as line-source (i.e., shown in Fig. 5b), from the time-averaged 2D map of the measured velocity fields (i.e., shown in Fig. 5c).

As shown in Fig. 5b, the skewed inflow is dominated by the  $v$ -velocity component, leading to highly turbulent flow along the upper part of the channel including the first two cavities (Fig. 5c). Along this part, the entering flow includes compound eddies, of various sizes, along the zone spanning the first building and the first cavity, that lead a skewed shear layer thereafter, towards the second cavity around which an eddy of flow recirculation occurs (Navas-Montilla et al. 2019). In the lower part of the channel (Fig. 5c), the flow is not as complex, exhibiting individual eddies in the bottom corner and in the cavities (i.e., from rectilinear shear layers along the cavity entrances, after the flow becoming rectilinear by the end of the first building).

The DG2-SWE and DG2-RANS- $k-\varepsilon$  simulations were conducted for resolutions that are much coarser than the optimal 0.003 m resolution of the turbulence length scale: the fine resolution was dictated by that of the skewed inflow (0.16 m or around  $0.46CL$ , using 84,016 cells) and the medium resolution was twice-coarser (0.32 m or around  $0.9CL$ , using 21,004 cells). Resolutions coarser than 0.32 m were not explored (exceed the  $CL$ ) nor finer than 0.16 m (lead to instabilities). The simulations started from zero initial flow conditions and in an extended domain’s length, of 11.4 m, and computational duration of 600 s to avoid interferences between the outflow boundary conditions and the turbulent-flow velocity fluctuations (could affect convergence).

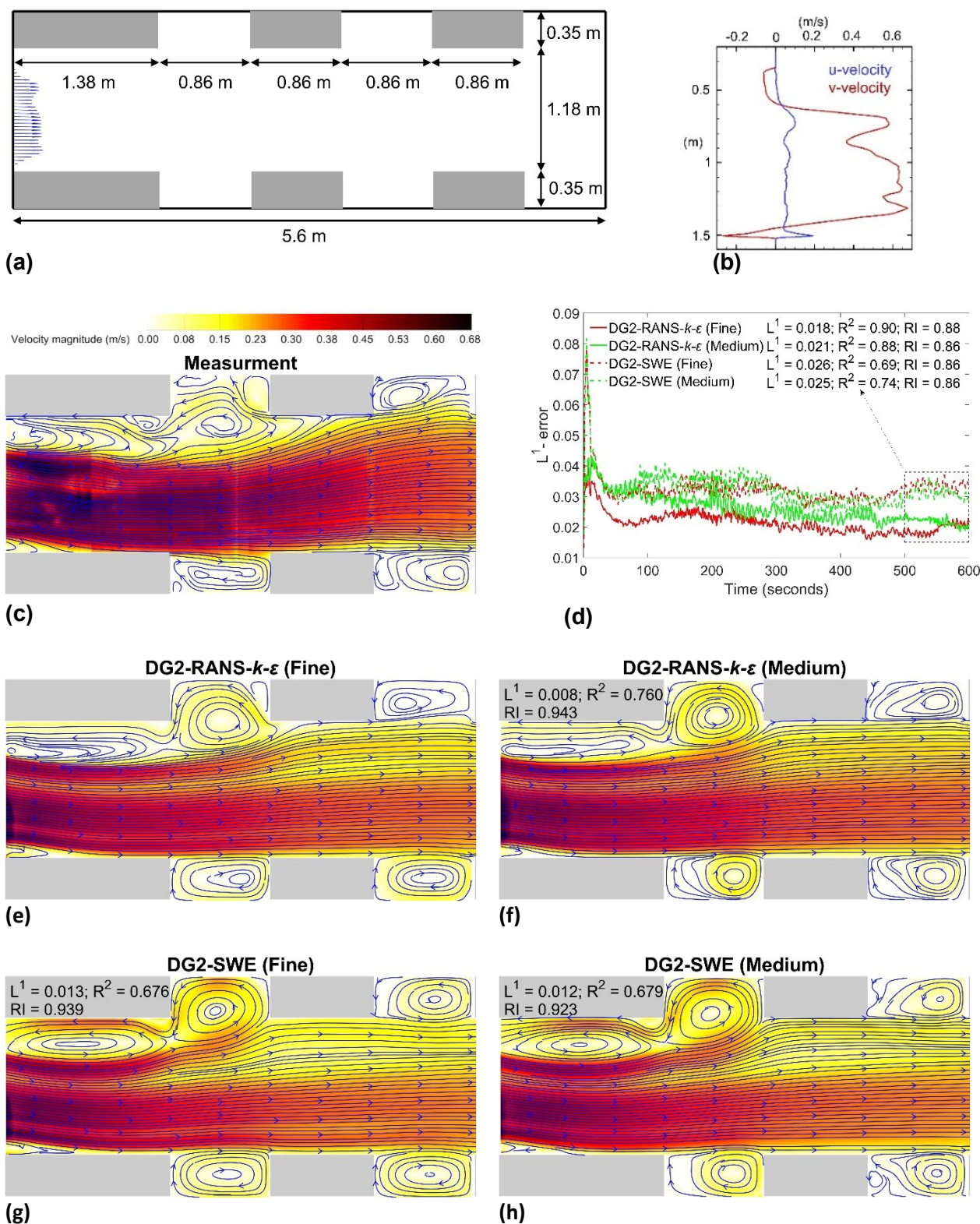


**Figure 5.** Recirculation flow in sharp building cavities: (a) channel with the cavities between rectangular buildings (the blue arrows indicate the inflow); (b) components of the velocity along the transverse cross-section ( $x = 0$ ) at the inlet. Panel (c): streamlines and magnitude of the measured velocity field (time-averaged experimentally) in the portion of the channel including the first two cavities; (d) time-series of  $L^1$ -error, calculated between the instantaneous 2D map of simulated velocity fields and the measured velocity field—the shown  $L^1$ ,  $R^2$  and  $RI$  scores were similarly calculated but only during the time-averaging interval [500 s, 600 s]; (e-h) streamlines and magnitude of time-averaged 2D maps from the fine- and medium-resolution DG2-RANS- $k-\epsilon$  and DG2-SWE simulations, respectively—the shown  $L^1$ ,  $R^2$  and  $RI$  were evaluated with reference to the simulation data shown in sub-figure 5e.

In Fig. 5d, the shown  $L^1$ -error time-series were calculated between the instantaneous 2D map of the simulated velocity fields and the (time-averaged 2D map of the) measured velocity field; whereas, the shown  $L^1$ ,  $R^2$  and  $RI$  scores were calculated based the on time-averaged 2D maps of the simulated velocity fields (i.e., after averaging of the instantaneous 2D maps of the simulated velocity fields during 500 s and 600 s). As seen in Fig. 5d, the fine-resolution DG2-RANS- $k-\epsilon$  simulation has the lowest and the steepest  $L^1$ -error, settling to values around 0.02; thus, produces instantaneous velocity fields with the closest variations with respect to the measured velocity field. The medium-resolution DG2-RANS- $k-\epsilon$  simulation has a slightly higher  $L^1$ -error, thus show a relatively wider range of variations in its instantaneous velocity fields. With the DG2-SWE simulations, the  $L^1$ -error at the fine resolution is only lower than at the medium resolution in the first 100 s, where it exhibits a similar range of variations as that the  $L^1$ -error for the medium-resolution DG2-RANS- $k-\epsilon$  simulation. After 100 s, the  $L^1$ -error with both the fine- and medium-resolution DG2-SWE simulations are close to each other and stagnate to values between 0.03 and 0.04, indicating that their prediction of velocity fields may have larger magnitudes compared to those predicted by the medium-resolution DG2-RANS- $k-\epsilon$  simulation. Ultimately, the DG2-SWE simulation tends to have a lower  $L^1$ -error at the medium resolution indicating that the medium-resolution simulation is likely to provide more reliable predictions than the fine-resolution simulation.

In Fig. 5d, the  $L^1$ ,  $R^2$  and  $RI$  scores compare the time-averaged 2D maps from the simulated velocity fields with respect to the 2D map of the measured data (experimentally time-averaged). Note that, the  $L^1$  scores (i.e., time-averaged  $L^1$ -error) are lower than the instantaneous  $L^1$ -error, suggesting that time-averaging renders the predicted velocity fields closer to the measured data. From the  $L^1$ ,  $R^2$  and  $RI$  scores, it can be inferred that: the fine-resolution DG2-RANS- $k-\epsilon$  simulation is the most accurate (i.e.,  $L^1 = 0.018$ ,  $R^2 = 0.90$  and  $RI = 0.88$ ), then comes the medium-resolution DG2-RANS- $k-\epsilon$  simulation (i.e.,  $L^1 = 0.021$ ,  $R^2 = 0.88$  and  $RI = 0.86$ ), followed by the medium-resolution DG2-SWE simulation (i.e.,  $L^1 = 0.025$ ,  $R^2 = 0.74$  and  $RI = 0.86$ ) that is more accurate than the fine-resolution DG2-SWE simulation (i.e.,  $L^1 = 0.026$ ,  $R^2 = 0.69$  and  $RI = 0.86$ ).

In Fig. 5e, the streamlines and magnitude of the time-averaged 2D map is shown for the fine-resolution DG2-RANS- $k-\epsilon$  simulation (used as the reference data to calculate the  $L^1$ ,  $R^2$  and  $RI$  scores shown in Fig. 5f-5h); and the maps for the medium-resolution DG2-RANS- $k-\epsilon$  simulation and the fine- and medium-resolution DG2-SWE simulations, shown in Fig. 5f to Fig. 5h, respectively. For the upper part of the channel, the size, position and near-zero velocity magnitude of the compound eddies—up to the second cavity—are best captured by the fine-resolution DG2-RANS- $k-\epsilon$  simulation (Fig. 5e vs. Fig. 5c). Comparatively, the medium-resolution

DG2-RANS- $k-\epsilon$  simulation (Fig. 5e vs. Fig. 5f) shows slight loss of accuracy in predicting the size of the compound eddies but still preserves the prediction of the near-zero velocity magnitude (i.e.,  $L^1 = 0.008$ ,  $R^2 = 0.76$  and  $RI = 0.94$ ). In contrast, the DG2-SWE simulations predict spurious velocity magnitudes around the compound eddies and change the location of the entering eddy (Fig. 5e vs. Fig. 5g and Fig. 5e vs. Fig. 5h).

In the lower part of less complex flow, all individual eddies are quite well-captured with all the DG2-RANS- $k-\epsilon$  and the DG2-SWE simulations (Fig. 5e vs. Fig. 5f-5h). However, the medium-resolution DG2-SWE simulation (i.e.,  $L^1 = 0.012$ ,  $R^2 = 0.679$  and  $RI = 0.92$ ) outperforms the fine-resolution DG2-SWE simulation (i.e.,  $L^1 = 0.013$ ,  $R^2 = 0.676$  and  $RI = 0.94$ ). Note that, some of the secondary eddies in the cavities seen in the measured velocity field (Fig. 5c) are not as clear in the simulated ones (Fig. 5e-5f), likely because numerical time-averaging is smoother than the experimental time-averaging.

The analysis of Fig. 5 indicates that the fine-resolution DG2-RANS- $k-\epsilon$  simulation seems inevitable to reproduce the size, magnitude, and positions of compound eddies. Notably, the fine resolution ( $0.46CL$ ) is here quite larger than resolution at the turbulence length scale ( $0.0086CL$ ), yet the fine-resolution DG2-RANS- $k-\epsilon$  solver could reproduce the compound eddies of various sizes. The medium-resolution ( $0.9CL$ ) DG2-RANS- $k-\epsilon$  simulation preserves an accurate prediction for the velocity magnitudes but can change the eddies' size and position. The DG2-SWE simulations acquire competitive predictions outside the zone of complex flow with compound eddies and is more accurate with the medium resolution.

#### 4.1.3. Flow past a square block in a diverting T-junction

This test case involves complex main-to-lateral flow separation in a T-junction system, made of three-branches (Fig. 6a). The main-branch flow develops compound eddies past the (dry, topographical) square block, located before the entrance into the side-branch. The compound eddies in the main-branch [shown in Fig. 6b based on the zoomed-in snapshot; reproduced by a three-dimensional (3D) RANS turbulent flow simulator (Mignot et al. 2013)] impacts the zone of flow separation as the flow diverts into the side-branch.

The T-junction system has a smooth and flatbed ( $n_M = 0.01$ ). In the computational domain, the main-branch's 5 cm square block ( $CL = 0.05$  m, Table 1) was spanned as a sharp-edged building as well as the two (rectangular) blocks along the lateral-branch (i.e., the grey blocks in Fig. 6a; assigned a high ground elevation). The main-branch has a rectilinear inflow of  $0.002 \text{ s}^{-1} \text{ m}^3$  and outflow water depths of 0.0451 and 0.0446 m in the lateral and downstream branches, respectively. In this test case ( $AR = 6.5$ , Table 1) the effects of turbulence

are less compared to the two previous test cases (much larger  $AR$ , Table 1). Therefore, without the square block, DG2-SWE simulations can reproduce the main feature of classical T-junction flow (Kesserwani et al. 2023), which is the eddy of recirculation in the lateral-branch (Shettar and Murthy 1996; Ramamurthy et al. 2007).

However, the compound eddies past the block render the flow too complex in the locality of the main-to-lateral flow separation (Fig. 6b). Still, the lateral-branch flow should involve the eddy of recirculation (Bazin et al. 2017), despite the main-branch flow exhibiting compound eddies (Sen et al. 2011; Zhang et al. 2022). In this case, DG2-SWE simulations fall short (Kesserwani et al. 2023) and DG2-RANS- $k-\epsilon$  simulations may not fully reproduce the (essentially 3D) flow features in the localities between the block and main-to-lateral flow separation (Dewals et al. 2023), even at resolutions finer than the turbulence length scale (0.006 m).

DG2-SWE and DG2-RANS- $k-\epsilon$  simulations were performed for the fine resolution (0.005 m or  $0.1CL$ , using 568,040 cells) used in Bazin et al. (2017), a twice-coarser medium resolution (0.01 m or  $0.2CL$ , using 142,100 cells) and a coarse resolution (0.02 m or  $0.4CL$ , using 35,525). A video of the fine-resolution DG2-RANS- $k-\epsilon$  simulation is on [https://www.seamlesswave.com/DG2\\_RANS](https://www.seamlesswave.com/DG2_RANS) (linked to the test-case image). All simulations started from zero initial flow conditions and were run for 250 s; convergence was assumed when the  $L^1$ -error  $\leq 10^{-4}$  (i.e.,  $L^1$ -error was calculated between the 2D maps of the water depth across two subsequent time-steps). Fig. 6c illustrates the plots of the  $L^1$ -error time-series for the fine-, medium- and coarse-resolution simulations. For the DG2-RANS- $k-\epsilon$  simulations, the finer the resolution the steeper the  $L^1$ -error decay and the lower its value. After 200 s, the  $L^1$ -error became  $\leq 10^{-8}$ ,  $10^{-5}$  and  $10^{-4}$  for the fine, medium and resolution, respectively, demonstrating a reliable convergence with the DG2-RANS- $k-\epsilon$  solver (steeper  $L^1$ -error decay with resolution refinement). In contrast, the DG2-SWE simulations lead to the  $L^1$ -error that stagnates at a magnitude  $> 10^{-4}$ , suggesting that the DG2-SWE solver cannot properly converge.

In Fig. 6d-6f and Fig. 6g-6i, the streamlines and magnitude of the time-averaged (during 200 and 250 s) 2D maps for the velocity fields are shown for the DG2-SWE and DG2-RANS- $k-\epsilon$  simulations, respectively, with the coarse-, medium- and fine-resolutions, each including the zoom-in view of the complex zone of flow separation (for comparison with that in Fig. 6b).

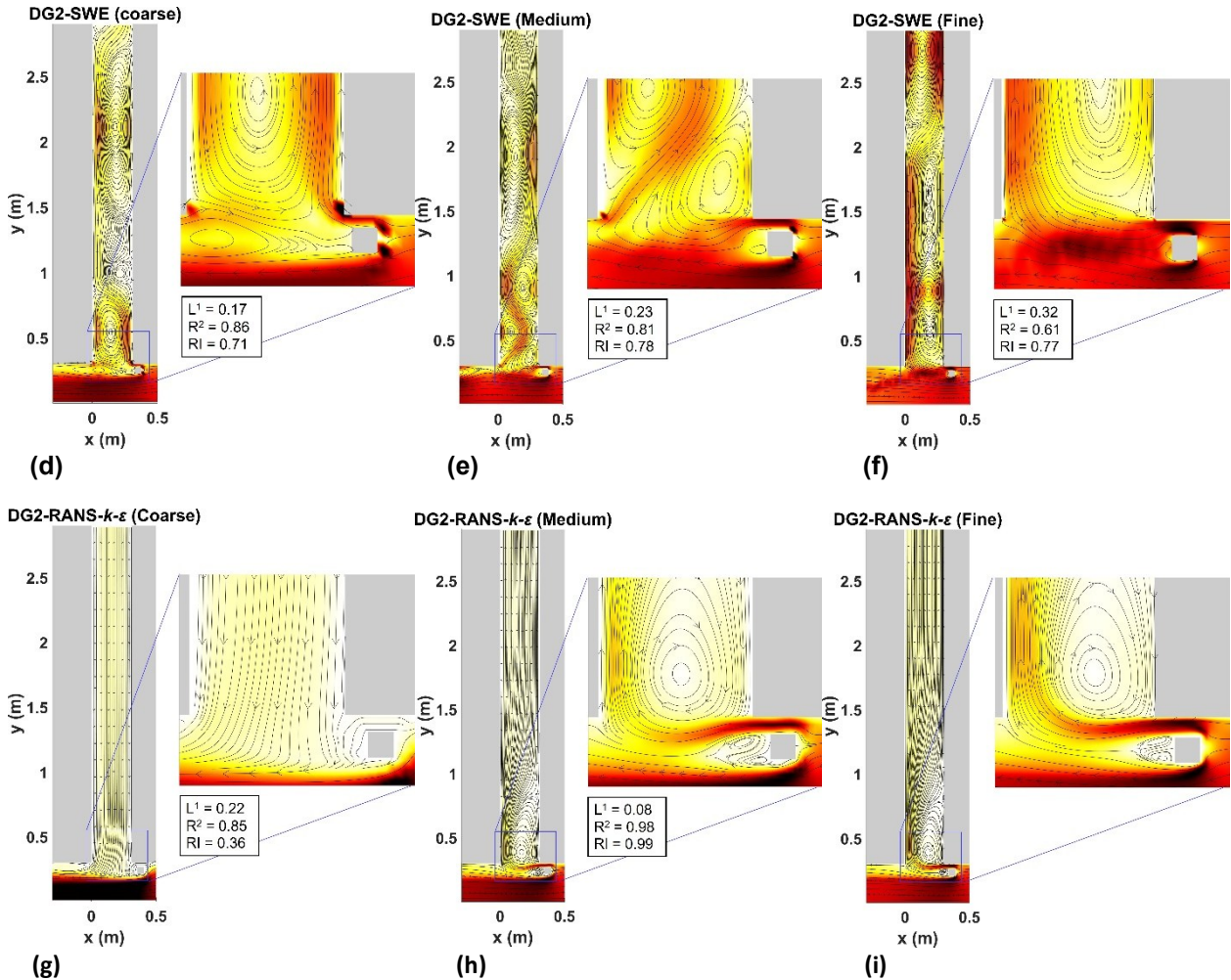
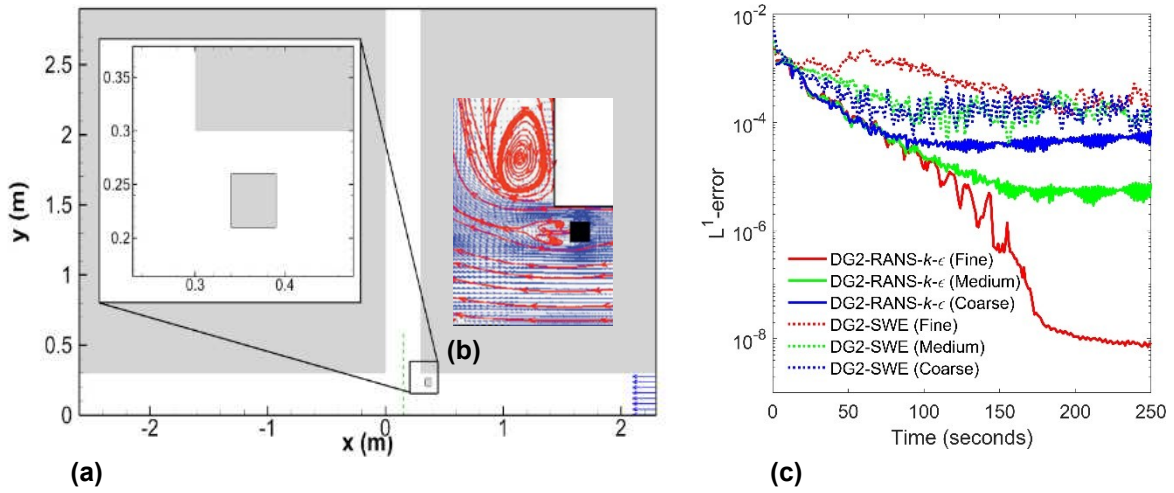


**Figure 6.** Flow past a square block in a diverting T-junction: (a) a sketch of the T-junction channel system made of three branches outside which a high dry wall (grey coloured) is generated (0.15 m height); the block in the main channel branch is also generated as a high dry wall (0.15 m height); (b) complex patterns of vortex structure interactions simulated by a 3D RANS turbulent flow solver [reprinted from Journal of Hydrology, Vol 494, Pages 10-19, © 2013, with permission from Elsevier]; (c)  $L^1$ -error convergence rates resulting from the coarse-, medium- and fine-resolution DG2-SWE and DG2-RANS- $k-\epsilon$  simulations; (d-f) and (g-i) show the velocity streamlines and magnitude for the time-averaged 2D maps (between 200 and 250 s) from the coarse-, medium- and fine-resolution DG2-SWE and DG2-RANS- $k-\epsilon$  simulations; in which  $L^1$ ,  $R^2$  and  $RI$  were evaluated with reference to the simulation data in sub-figure 6i.

As can be seen in Fig. 6d-6f, the DG2-SWE simulations fail to reproduce the patterns in the complex flow zone. The coarse-resolution DG2-RANS- $k-\epsilon$  simulation also fails, even more than the coarse-resolution DG2-SWE simulation (Fig. 6d vs. Fig. 6g): the former overlooks the high-magnitude velocity past the block and the eddy of recirculation in the lateral branch, which could both be somewhat detected by the latter. Hence, there is no benefit of using the DG2-RANS- $k-\epsilon$  simulation over the DG2-SWE simulation at the coarse resolution, nor from using a finer resolution DG2-SWE simulation.

In contrast, the medium- and fine-resolution DG2-RANS- $k-\epsilon$  simulations detect the presence of the high velocity magnitude between the main-branch's side wall and block, the compound eddies past the block, and the lateral-branch's eddy of flow recirculation (Fig. 6d-6-i); therefore, resulting in unrivalled predictions from the medium resolution.

The reference fine-resolution DG2-RANS- $k-\epsilon$  prediction (Fig. 6i) is best reproduced by the medium-resolution DG2-RANS- $k-\epsilon$  simulation (i.e.,  $L^1 = 0.08$ ,  $R^2 = 0.98$  and  $RI = 0.99$ ) and worst reproduced by coarse-resolution DG2-RANS- $k-\epsilon$  simulation (i.e., an uncompetitive  $RI = 0.36$ ). Comparatively, the coarse-resolution DG2-SWE simulation (i.e.,  $L^1 = 0.17$ ,  $R^2 = 0.86$  and  $RI = 0.71$ ) is better than the medium- and fine-resolution DG2-SWE simulations (i.e.,  $L^1$  increases to 0.23 and to 0.32, respectively; while  $R^2$  decreasing to 0.81 and to 0.61). Hence, the DG2-SWE solver may only be useful at the coarser resolution.

Fig. 7a and 7b include the plots of the experimentally measured (Bazin et al. 2017)  $u$ - and  $v$ -velocity profiles and those from the DG2-SWE and DG2-RANS- $k-\epsilon$  simulations: these profiles were extracted along the cross-section  $x = 0.15$  m, shown as a vertical dashed line in Fig. 6a, located in the zone of main-to-lateral flow separation. Also, the  $R^2$  scores shown in Figs. 7a and 7b were calculated with reference to the measured data. Along the cross-section  $x = 0.15$  m ( $0 \text{ m} \leq y \leq 0.6 \text{ m}$ ), the main-branch flow spans  $0 \text{ m} \leq y \leq 0.2 \text{ m}$ , the lateral-branch flow spans  $0.4 \text{ m} \leq y \leq 0.6 \text{ m}$ , and  $0.2 \text{ m} \leq y \leq 0.4 \text{ m}$  spans the zone of complex flow separation.

As shown in Fig. 7a, the measured  $u$ -velocity profile of the main-branch flow ( $0 \text{ m} \leq y \leq 0.2 \text{ m}$ ) is best reproduced by the fine- and medium-resolution DG2-RANS- $k-\epsilon$  simulations, and somewhat by the coarse-resolution DG2-SWE simulation. The fine- and medium-resolution DG2-SWE simulations overpredict the measured profile and the coarse-resolution DG2-RANS- $k-\epsilon$  simulation underpredicts it. As for the measured  $u$ -velocity profile in the lateral-branch flow ( $0.4 \text{ m} \leq y \leq 0.6 \text{ m}$ ), the near-zero velocity (inside the dead zone) is better reproduced by the fine- and the medium-resolution DG2-RANS- $k-\epsilon$  simulations compared to any other simulation. Within the zone of complex flow ( $0.2 \text{ m} \leq y \leq 0.4 \text{ m}$ ), all simulated  $u$ -velocity profiles are not very

close to the measured profile; however, only the fine-resolution DG2-RANS- $k-\epsilon$  simulation predicts a rising limb that is bounded by the variations seen in the measured profile. This is likely why the latter simulation has the highest  $R^2 = 0.98$ , with respect to the measured profile compared to the other simulations, with  $0.76 \leq R^2 \leq 0.94$ , suggesting that they have slightly less accurate predictions for the  $u$ -velocity profile.

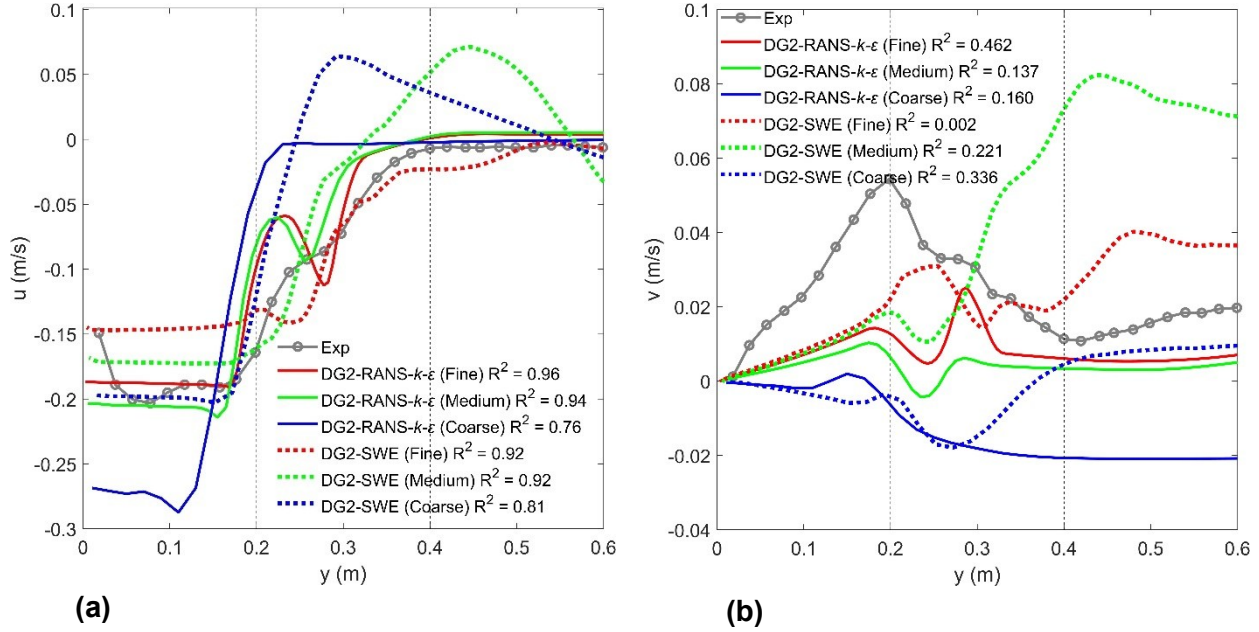


**Figure 7.** Flow past a square block in a diverting T-junction: (a) and (b) include a comparison between the measured and simulated  $u$ - and  $v$ -velocity spatial profiles [along the centreline ( $x = 0.15$ ) marked as a dashed line in Fig. 6a]; the main- and lateral-branch flows span the zones:  $0 \leq y \leq 0.2$  and  $0.4 \leq y \leq 0.6$ , respectively; whereas the zone of complex main-to-lateral flow separation spans  $0.2 \leq y \leq 0.4$ ; The  $R^2$  scores shown were calculated with reference to the measured data.

The measured  $v$ -velocity profile is found to be more challenging to reproduce by both DG2-RANS- $k-\epsilon$  and DG2-SWE simulations. As shown in Fig. 7b, the coarse-resolution DG2-RANS- $k-\epsilon$  and DG2-SWE simulations fail to capture the rising limb of the main-branch flow ( $0 \text{ m} \leq y \leq 0.2 \text{ m}$ ), exhibiting spuriously negative predictions; whereas, only the fine- and medium-resolution DG2-RANS- $k-\epsilon$  simulations could trail the lateral-branch flow ( $0.4 \text{ m} \leq y \leq 0.6 \text{ m}$ ), involving a slightly increasing near-to-zero velocity. Again, none of the DG2-RANS- $k-\epsilon$  and DG2-SWE simulations yield a very close agreement with the measured profile in the zone of complex flow ( $0.2 \text{ m} \leq y \leq 0.4 \text{ m}$ ); however, the fine-resolution DG2-RANS- $k-\epsilon$  simulation can be said to be the most accurate: it has the highest  $R^2 = 0.42$  with respect to the measured profile and could predict the velocity recovery rate (along  $y > 0.3 \text{ m}$ ) more accurately than any of the other simulations. The DG2-SWE simulations have uncompetitive  $R^2$  scores (i.e., all of which resulted from a negative coefficient of correlation), suggesting that they predict the velocity in the opposite direction in some location (compared to the measured profile). The medium- and coarse-resolution DG2-RANS- $k-\epsilon$  simulations have also low  $R^2$  scores (i.e., that resulted from positive coefficient of correlation), also suggesting uncompetitive predictions when reproducing

the  $v$ -velocity profile. Arguably, as concluded in Dewals et al. (2023), the accurate reproduction of the velocity components in such a complex locality—where the flow is impacted by the compounded eddies past the block—is beyond the capability of 2D turbulent flow simulators. In such a case, only the fine-resolution DG2-RANS- $k$ - $\epsilon$  simulation can acquire fairly accurate approximations of the complex 3D flow processes taking place, and could be used as an alternative to more expensive 3D turbulent flow simulators (Ramamurthy et al. 2007; Li and Zeng 2009; Mignot et al. 2013; Jin et al. 2023; Pandey and Mohapatra 2023).

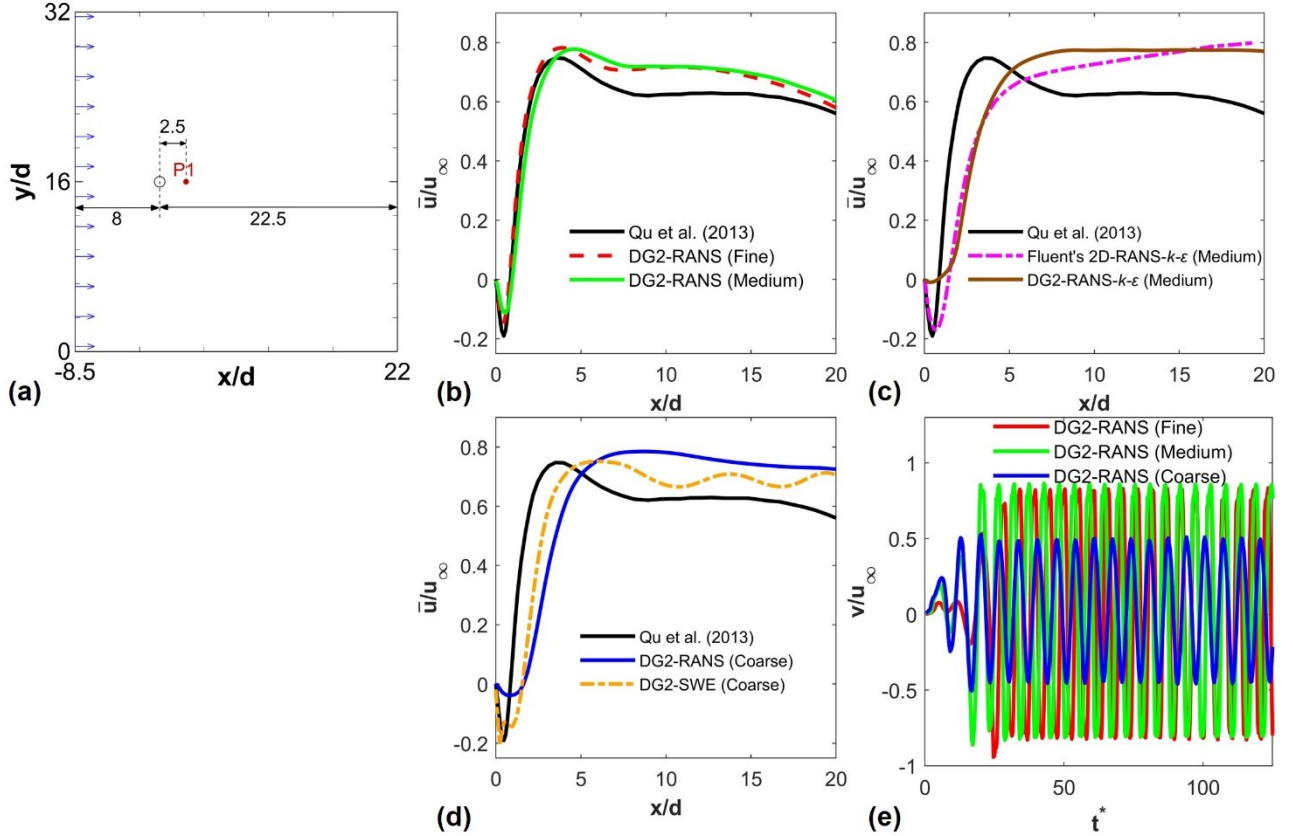


**Figure 8.** Wake past a cylinder: (a) the domain including the 4 mm diameter cylinder and showing the rectilinear inflow (using arrows); (b-d) time-averaged, scaled longitudinal velocity ( $\bar{u}/u_\infty$ ) profiles, along the centreline cross the cylinder ( $y/d = 16$ ), from the fine- and medium-resolution laminar DG2-RANS simulations [sub-figure (b)], the medium-resolution DG2-RANS- $k$ - $\epsilon$  turbulent flow and Fluent’s 2D-RANS- $k$ - $\epsilon$  simulations [sub-figure (c)], and the coarse-resolution DG2-RANS and DG2-SWE simulations [sub-figure (d)]— all compared to the reference profile (Qu et al. 2013); and, (e) time-series of the scaled transverse velocity ( $v/u_\infty$ ) at point P1 [sub-figure (a)], used to analyse tracking of vortex-shedding frequency and magnitude for the fine-, medium- and coarse-resolution laminar DG2-RANS simulations.

## 4.2. Laminar flows

### 4.2.1. Wake past a cylinder

A laminar wake flow past a cylinder of diameter  $d = 4$  mm ( $CL = 0.004$  m, Table 1) is reproduced for a  $Re = 200$  [i.e., here and in Sec. 4.2.2,  $Re$  denotes the cylinder Reynolds number (Rajani et al. 2009; Qu et al. 2013; Sun et al. 2023)]. The cylinder area (i.e., assigned a high ground elevation) is around the middle of a flat and smooth domain ( $n_M = 0.01$ ), with dimensions of  $30.5d \times 32d$ , scaled with respect to  $d$  (the portion shown in

Fig. 8a). These dimensions were extended (computationally) to ensure that inflow and outflow boundaries remain far from the near-cylinder region, thereby avoid possible flow boundary impacts on the wake structures past the cylinder. The steady inflow has a velocity of  $u_\infty = 0.05 \text{ s m}^{-1}$ , with respect to which the velocity field components were scaled for analysis based on the scaled time unit,  $t^* = t u_\infty / d$ .

Three DG2-RANS simulations were run, to include at least 50 vortex-shedding wake period cycles (Sun et al. 2023), for coarse (1 mm, or  $0.25CL$ , using 15,616 cells), medium (0.5 mm, or  $0.125CL$ , using 62,464 cells) and fine (0.25 mm, or  $0.0625CL$ , 249,856 cells) resolutions ( $CL = d$ , Table 1). Further, medium-resolution DG2-RANS- $k-\epsilon$  and Fluent's 2D-RANS- $k-\epsilon$  simulations were run. In Fig. 8b-8d, the simulated centreline (i.e., along  $y/d = 0$ ) profiles of the time-averaged longitudinal velocity component are plotted and compared with a reference profile [i.e., a 2D-RANS simulation at a cylinder resolution of  $0.0001CL$  (Qu et al. 2013)] and considering the profile from the coarse-resolution DG2-SWE simulation (Sun et al. 2023).

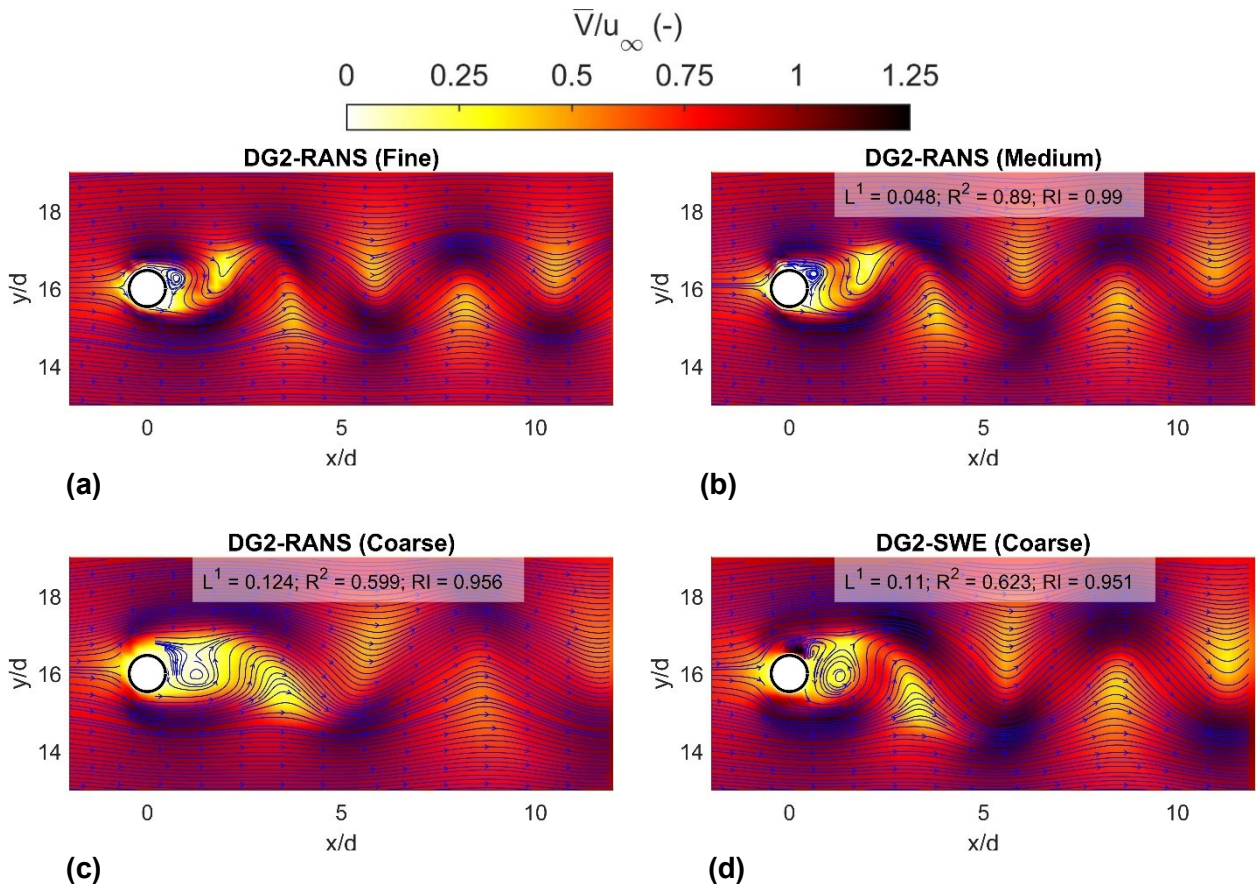


**Figure 9.** Wake past a cylinder. Streamlines and magnitude of the 2D maps of instantaneous velocity fields (i.e., after 9 vortex-shedding wake cycles) for the by the laminar DG2-RANS simulations at the (a) fine, (b) medium, and (c) coarse resolutions; and (d) by the coarse-resolution DG2-SWE simulation; with  $L^1$ ,  $R^2$  and  $RI$  evaluated with reference to the simulation data in sub-figure 9a.

As can be detected in Fig. 8b-8d, the fine-resolution DG2-RANS simulation has the best agreement with the reference profile. This agreement is acceptably preserved by the medium-resolution DG2-RANS

simulation (Fig. 8b), in contrast to with the medium-resolution DG2-RANS- $k-\epsilon$  and Fluent's 2D-RANS- $k-\epsilon$  simulations that fall short (Fig. 8c). The coarse-resolution DG2-RANS simulation also falls short (Fig. 8d), by exhibiting similar shortcomings (Fig. 8c-8d): spuriously prolonged velocity recovery rate and recirculation length in the near-cylinder region ( $x/d < 5$ ) and a spuriously flattened profile in far-wake region ( $x/d \geq 5$ ), which are, somewhat, better predicted by coarser-resolution DG2-SWE simulation (Fig. 8d).

In Fig. 8e, the time-series of the transverse velocity profile at point P1 (shown in Fig. 8a) are plotted for the fine-, medium- and coarse-resolution DG2-RANS simulations. From these time-series, vortex-shedding frequency,  $f_s$ , can be calculated for evaluating the Strouhal number,  $S_t = f_s d / u_\infty$ . The fine-resolution DG2-RANS simulation predicts a velocity profile (Fig. 8e), leading to  $S_t = 19$  in agreement with the reference  $S_t = 0.19$  (Rajani et al. 2009; Qu et al. 2013). This agreement is acceptably preserved by the medium-resolution DG2-RANS simulation, leading a fairly close  $S_t = 18$ , in contrast to with the coarse-resolution DG2-RANS simulation. As can seen in Fig. 8e, the latter simulation manifested in a relatively lower velocity magnitude and a relatively unaligned frequency, leading to  $S_t = 0.15$  that is closer to that from the coarse-resolution DG2-SWE simulation (Sun et al. 2023).

In Fig. 9, the 2D maps of the simulated (instantaneous) velocity streamlines and magnitude [i.e., the time instant after 9 vortex-shedding cycles passed (Sun et al. 2023)] are compared, considering: the fine-, medium- and coarse-resolution DG2-RANS simulations (Fig. 9a-9b) and the coarse-resolution DG2-SWE simulation (Fig. 9d)—the  $L^1$ ,  $R^2$  and  $RI$  scores in Fig. 9b-9d are evaluated with reference to the data shown in Fig. 9a. In the near-cylinder region, the coarse-resolution DG2-RANS and DG2-SWE simulations predict unaligned wake position and extent, compared to those predicted by the fine-resolution DG2-RANS simulation [and to those by the medium-resolution DG2-RANS simulation, leading to similar velocity streamlines and magnitude as the fine-resolution DG2-RANS simulation ( $L^1 = 0.048$ ,  $R^2 = 0.89$  and  $RI = 0.99$ )]. Outside this locality, in the far-wake region, the velocity streamlines and magnitude are better predicted by the coarse-resolution DG2-SWE simulation ( $L^1 = 0.11$ ,  $R^2 = 0.623$  and  $RI = 0.951$ ) compared to the coarse-resolution DG2-RANS simulation ( $L^1 = 0.124$ ,  $R^2 = 0.599$  and  $RI = 0.956$ ).

Overall, the analysis of Figs. 8 and 9 suggests a reliable use of the DG2-RANS laminar flow solver from the medium resolution, such as to reproduce wake evolutions and interactions in the near-cylinder region (Sec. 4.2.2). It also suggests preferring the DG2-SWE solver over DG2-RANS laminar flow solver when conducting simulations at the coarse resolution (Sec. 4.2.2).

#### 4.2.2. Wake interactions past many cylinders

The medium-resolution DG2-RANS simulation (0.5 mm or  $0.125CL$ ,  $CL = d$ ) is further explored to reproduce wake evolutions and interactions past many randomly distributed cylinders, over 50 vortex-shedding cycles. A video of the medium-resolution DG2-RANS simulation is on [https://www.seamlesswave.com/DG2\\_RANS](https://www.seamlesswave.com/DG2_RANS) (linked to the test-case image). The cylinders are identical, of diameter  $d = 4$  mm, and are located in a  $3750d \times 75d$  computational flume [i.e., dry cells inside the cylinder areas (Fig. 10a) were assigned a high ground elevation— see test-case image on [https://www.seamlesswave.com/DG2\\_RANS](https://www.seamlesswave.com/DG2_RANS)]. The flume had a longitudinal slope of  $4.6 \times 10^{-4} \text{ m m}^{-1}$  and a rough bed ( $n_M = 0.045$ ) to keep the uniform water depth, following the experiments made in a flume at the University of Warwick (Sun et al. 2023), leading an inflow velocity of  $u_\infty = 0.06 \text{ s m}^{-1}$ . The cylinders were only generated along a  $1875d$  length of the domain, as duplicates of a randomly generated cylinder distribution on a  $625d \times 75d$  baseplate. The part of the computational flume including the cylinders, along  $1875d$ , is here referred to as “cylinder array section”. Surface PIV measurements of instantaneous  $u$ - and  $v$ -velocity data (Corredor-Garcia et al. 2021) were collected for the red-framed area (i.e., the  $137.5d \times 75d$  area shown in Fig. 10a), that is  $1332.5d$  far from the start of the cylinder array section.

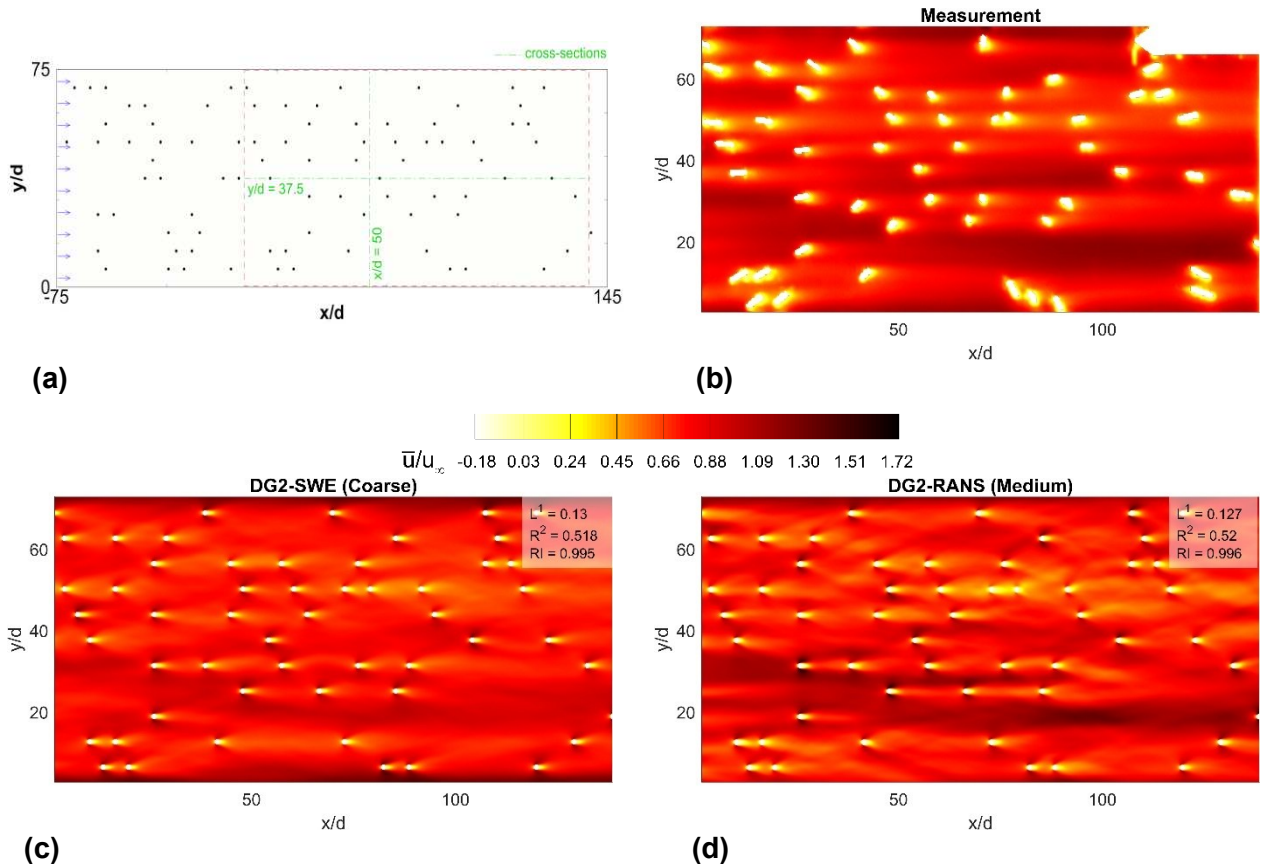


**Figure 10.** Wake interactions past many cylinders: (a) a part of the laboratory flume including the cylinder array section (with randomly distributed cylinders) and showing the direction of the inflow (arrows); (b) the time-averaged, scaled longitudinal velocity ( $\bar{u}/u_\infty$ ) map of the measured data, covering in the red-framed portion in sub-figure (a); (c) and (d)

include  $\bar{u}/u_\infty$  maps from the coarse-resolution DG2-SWE simulation and the medium-resolution DG2-RANS simulation, respectively; with  $L^1$ ,  $R^2$  and  $RI$  evaluated with reference to the measured data in sub-figure 9b.

In Fig. 10b-10d, the time-averaged 2D maps of the  $u$ -velocity components are compared, considering: the measured data (Fig. 10b) versus the simulated fields from the coarse-resolution DG2-SWE simulation (Fig. 10c) and the medium-resolution DG2-RANS simulation (Fig. 10d)—the shown  $L^1$ ,  $R^2$  and  $RI$  scores within were calculated with reference to the time-averaged measured data (Fig. 10b). Since the time-averaged 2D maps of the  $v$ -velocity component were (visually) very similar (not shown), the prediction of the  $v$ -velocity component was based on a quantitative analysis of the average and standard deviation of the  $S_t$  (i.e., sampled from all the  $v$ -velocity time-series at a  $2.5d$  distance past and along all the cylinders).

As can be seen in Fig. 10b-10d, the locality of high  $u$ -velocity preferential flow in the open area ( $10 < y/d < 30$ ) is much better captured by the medium-resolution DG2-RANS simulation as compared to the coarse-resolution DG2-SWE simulation. This improvement is expected as the former simulation included the effects of the viscous stresses, leading to better  $L^1$ ,  $R^2$  and  $RI$  scores. For the predictability of the  $v$ -velocity component, the  $S_t$  range sampled from the medium-resolution DG2-RANS simulation, of  $0.15 \pm 0.081$ , is closer to the range sampled from the measured data, of  $0.2 \pm 0.055$ , than that, of  $0.11 \pm 0.057$ , sampled from the coarse-resolution DG2-SWE simulation. This indicates the medium-resolution DG2-RANS simulation provides better prediction of the  $v$ -velocity component too.

Note that, the comparisons made are quite rough since the measured data was subject to experimental discrepancies, mostly due to uncorrected projection bias that shifted the measured cylinder positions; and the simulated data to numerical discrepancies, mostly due to squared-grid representation of the cylinders. Still, the results are quite illustrative of the capability of the medium-resolution DG2-RANS simulation to better capture the preferential longitudinal flow and wake interactions than the coarse-resolution DG2-SWE simulation.

## 5. Conclusions and recommendations

A novel second-order Discontinuous Galerkin (DG2) solver of the advective-diffusive  $5 \times 5$  RANS- $k-\varepsilon$  system—the three Partial Differential Equations (PDEs) of the Reynolds-Averaged Navier–Stokes incorporating the  $k-\varepsilon$  model and two associated PDEs for the update of the turbulent-flow variables—was developed (DG2-RANS- $k-\varepsilon$ ). In so doing, the  $5 \times 5$  RANS- $k-\varepsilon$  system was, first, transformed to become an advective-dominated  $13 \times 13$  RANS- $k-\varepsilon$  system, and, then, solved by extending the “slope-decoupled” advective DG2 solver’s formulation and adapting robustness treatments for the mean-flow variables—the localised treatments integrating steep wet-

dry fronts and local slope-limiting featuring in the DG2 solver the shallow water equations (DG2-SWE). A new combination of stability/positivity-preserving treatments for the turbulent-flow quantities was also needed to ensure the overall reliability of the DG2-RANS- $k$ - $\varepsilon$  solver.

Five experimental benchmarks were used to evaluate the capability of the DG2-RANS- $k$ - $\varepsilon$  turbulent flow solver and DG2-RANS laminar flow solver, jointly with that of the DG2-SWE solver. The benchmarks were simulated considering coarse, medium and fine resolutions—between the Characteristic length ( $CL$ ) and the turbulence length scale (benchmark-specific). The evaluation was based on qualitative and quantitative comparisons of the simulated spatial velocity fields (instantaneous and/or time-averaged) against the benchmark-specific measured data and against the most accurate simulation data [from the fine-resolution DG2-RANS- $k$ - $\varepsilon$  (resp. DG2-RANS) simulations in the turbulent flow (resp. laminar flow) benchmarks].

For the turbulent flow simulations, the DG2-RANS- $k$ - $\varepsilon$  solver could further replicate compound eddies from the medium resolution, which cannot otherwise be captured by the DG2-SWE solver. For the laminar flow simulations, the DG2-RANS solver (without the  $k$ - $\varepsilon$  model) could better reproduce the evolution and/or interaction of wake structures—also from the medium resolution. In both of the turbulent flow and the laminar flow simulations, the DG2-SWE solver yielded its best predictions at the coarsest resolution, at which both the DG2-RANS- $k$ - $\varepsilon$  turbulent flow solver and laminar DG2-RANS solver fell short.

The open-source code of the DG2-RANS- $k$ - $\varepsilon$  turbulent flow solver (thereby, the DG2-RANS laminar flow solver) is available within a new release of the LISFLOOD-FP hydraulic software environment—with the benchmark-specific initial condition set up files—to run parallel simulations on the CPU or on the GPU (DOI: <https://doi.org/10.5281/zenodo.7628739>). The operational (memory) costs in the DG2-RANS/DG2-RANS- $k$ - $\varepsilon$  solver (21/39 cellwise degrees of freedom) are much higher compared to those in the DG2-SWE solver (9 cellwise degrees of freedom). Consequently, the runtimes of the DG2-RANS/DG2-RANS- $k$ - $\varepsilon$  solver reduced by 7-fold with doubling in resolution, from fine to medium [on CPU (10 threads) or on GPU (V100 card)], and further by 2-to-6-fold with the GPU runs—despite on unusually small-sized grids (20k-to-250k cells).

The evaluation of both the predictive accuracy and runtime efficiency suggests preferring the medium resolution, over the fine resolution, to make practical DG2-RANS laminar flow simulations and DG2-RANS- $k$ - $\varepsilon$  turbulent flow simulations. However, the fine resolution (below the turbulence length scale) may be needed with the DG2-RANS- $k$ - $\varepsilon$  turbulent flow solver (e.g., if applied as an alternative to three-dimensional turbulent flow simulators) to approximate highly-turbulent localities involving compound eddies of various sizes.

## Appendix A.

### A.1. Inter-cell evaluation of the advective fluxes

Following a similar derivation from the, slope-decoupled, advective DG2 formulation (Kesserwani et al. 2018, Shaw et al. 2021), the DG2 discretisation of the gradients,  $\partial Q/\partial x$  and  $\partial Q/\partial y$ , of any advective flux component  $Q \in I_{inviscid} \cup I_{viscous}$  (see Eq. 12) can be derived and simplified to be expressed, over the sample cell, as:

$$\begin{aligned}
 (\partial Q/\partial x)_j^0 &= \frac{1}{\Delta x} (\tilde{Q}_E - \tilde{Q}_W) & (\partial Q/\partial y)_j^0 &= \frac{1}{\Delta y} (\tilde{Q}_N - \tilde{Q}_S) \\
 (\partial Q/\partial x)_j^{1x} &= \frac{\sqrt{3}}{\Delta x} (\tilde{Q}_E + \tilde{Q}_W - Q_{Gx2} - Q_{Gx1}) & (\partial Q/\partial y)_j^{1x} &= 0 \\
 (\partial Q/\partial x)_j^{1y} &= 0 & (\partial Q/\partial y)_j^{1y} &= \frac{\sqrt{3}}{\Delta y} (\tilde{Q}_N + \tilde{Q}_S - Q_{Gy2} - Q_{Gy1})
 \end{aligned} \tag{A1}$$

In Eq. (A1),  $Q_{Gx1}$ ,  $Q_{Gx2}$ ,  $Q_{Gy1}$  and  $Q_{Gy2}$  are component-wise physical flux evaluations at the inner-cell values  $W_j(Gx1, t)$ ,  $W_j(Gx2, t)$ ,  $W_j(Gy1, t)$  and  $W_j(Gy2, t)$ , respectively (Fig. 1 and Eq. 11). Whereas,  $\tilde{Q}_E$  and  $\tilde{Q}_W$ , in  $(\partial Q/\partial x)_j^K$ , and  $\tilde{Q}_N$  and  $\tilde{Q}_S$ , in  $(\partial Q/\partial y)_j^K$ , are inter-cell approximate numerical fluxes that must be evaluated across faces  $E$  and  $W$ , and faces  $N$  and  $S$ , respectively (Fig. 1)—these faces are shared by the four cells adjacent to the sample cell. Next, only the discretisation of  $(\partial Q/\partial x)_j^K$  is described, since that of  $(\partial Q/\partial y)_j^K$  is similar, for which it suffices to describe the evaluation of  $\tilde{Q}_E$ , since  $\tilde{Q}_W$  can be evaluated in a similar way.

The involvement of a two-argument numerical flux function is key to the evaluation of  $\tilde{Q}_E$  in a way that links the inner-cell limit at  $E$  [i.e., from the DG2 approximation at the sample cell in  $\mathbf{W}(E, t)$ ] to the outer-cell limit at  $E$  [i.e., from the DG2 approximation outside the sample cell, denoted hereafter by  $\mathbf{W}^+(E, t)$ ].

When  $Q \in I_{inviscid}$  (Eq. 12), the numerical flux function is based on a Riemann solver for properly linking potentially discontinuous limits (Toro 2010). The *Local Lax Friedrich* Riemann solver was used to reduce the computational costs (Kesserwani et al. 2008; Hejranfar and Hajihassanpour 2017; Hajihassanpour and Hejranfar 2022), from which  $\tilde{Q}_E$  is evaluated as:

$$\tilde{Q}_E = \frac{1}{2} (Q_E^+ + Q_E) - \lambda_{\max} [W_j^+(E, t) - W_j(E, t)] \tag{A2}$$

In Eq. (A2),  $W_j(E, t)$  and  $W_j^+(E, t)$  are the associated component of the inner-cell and outer-cell limits at  $E$ , respectively;  $Q_E$  and  $Q_E^+$  are physical flux evaluations at  $W_j(E, t)$  and  $W_j^+(E, t)$ ; and,  $\lambda_{\max}$  is the maximum local characteristic speed, given as  $\lambda_{\max} = \max \left[ \sqrt{(u_E)^2 + (v_E)^2} + \sqrt{gh_E}, \sqrt{(u_E^+)^2 + (v_E^+)^2} + \sqrt{gh_E^+} \right]$ , in which  $u_E$ ,  $v_E$  and  $h_E$  are evaluated from within  $\mathbf{W}(E, t)$ , and  $u_E^+$ ,  $v_E^+$  and  $h_E^+$  from within  $\mathbf{W}^+(E, t)$ . Note that when,  $Q$  represents a turbulent-flow inviscid flux component the wave celerity terms in  $\lambda_{\max}$  must be removed.

When  $Q \in I_{viscous}$  (Eq. 12), central flux averaging (Hajihassanpour and Hejranfar 2020, 2022) can be used to define the numerical flux function, from which  $\tilde{Q}_E$  is evaluated as:

$$\tilde{Q}_E = \frac{1}{2}(Q_E^+ + Q_E) \quad (A3)$$

Note that, in Eq. (A2), any of the first five components in  $W_j(E, t)$  and  $W_j^+(E, t)$  can be involved ( $j = 1, \dots, 5$ ); but, in Eq. (A3), any of all the thirteen components can be involved ( $j = 1, \dots, 13$ ).

When face  $E$  is located at a boundary line (enclosing the computational domain) a *ghost boundary cell* is introduced to assign the outer-cell limits [i.e., involved in  $\mathbf{W}^+(E, t)$ , namely for:  $h_E^+$ ,  $u_E^+$ ,  $v_E^+$ ,  $\varepsilon_E^+$ ,  $k_E^+$ ,  $(A_{u_x})_E^+$ ,  $(A_{v_x})_E^+$ ,  $(A_{u_y})_E^+$ ,  $(A_{v_y})_E^+$ ,  $(A_{k_x})_E^+$ ,  $(A_{k_y})_E^+$ ,  $(A_{\varepsilon_x})_E^+$  and  $(A_{\varepsilon_y})_E^+$ ]. Assigning these outer-cell limits is either based on extrapolation of components at the inner-cell limits [i.e., in  $\mathbf{W}(E, t)$ ] or on given physical values, depending on what a boundary line represents, based on three user-specified choices: ‘‘Inflow’’ (Eq. A4), ‘‘Outflow’’ (Eq. A5) or ‘‘Closed’’ (Eq. A6), as described in Eqs. (A4-A6):

Inflow	$h_E^+ = h_E$ $u_E^+ = u_{BC}$ $(A_{u_x})_E^+ = (A_{u_x})_E$ $(A_{u_y})_E^+ = -(A_{u_y})_E$ $k_E^+ = k_{BC}$ $(A_{k_x})_E^+ = (A_{k_x})_E$ $(A_{k_y})_E^+ = -(A_{k_y})_E$	$v_E^+ = v_{BC}$ $(A_{v_x})_E^+ = (A_{v_x})_E$ $(A_{v_y})_E^+ = -(A_{v_y})_E$ $\varepsilon_E^+ = \varepsilon_{BC}$ $(A_{\varepsilon_x})_E^+ = (A_{\varepsilon_x})_E$ $(A_{\varepsilon_y})_E^+ = -(A_{\varepsilon_y})_E$	(A4)
Outflow	$h_E^+ = h_{BC}$ $u_E^+ = u_E$ $(A_{u_x})_E^+ = -(A_{u_x})_E$ $(A_{u_y})_E^+ = (A_{u_y})_E$ $k_E^+ = k_E$ $(A_{k_x})_E^+ = -(A_{k_x})_E$ $(A_{k_y})_E^+ = (A_{k_y})_E$	$v_E^+ = v_E$ $(A_{v_x})_E^+ = -(A_{v_x})_E$ $(A_{v_y})_E^+ = (A_{v_y})_E$ $\varepsilon_E^+ = \varepsilon_E$ $(A_{\varepsilon_x})_E^+ = -(A_{\varepsilon_x})_E$ $(A_{\varepsilon_y})_E^+ = (A_{\varepsilon_y})_E$	(A5)
Closed	$h_E^+ = h_E$ $u_E^+ = -u_E$ $(A_{u_x})_E^+ = (A_{u_x})_E$ $(A_{u_y})_E^+ = -(A_{u_y})_E$ $k_E^+ = k_{tol}$ $(A_{k_x})_E^+ = (A_{k_x})_E$ $(A_{k_y})_E^+ = -(A_{k_y})_E$	$v_E^+ = v_E$ $(A_{v_x})_E^+ = -(A_{v_x})_E$ $(A_{v_y})_E^+ = (A_{v_y})_E$ $\varepsilon_E^+ = \varepsilon_{tol}$ $(A_{\varepsilon_x})_E^+ = (A_{\varepsilon_x})_E$ $(A_{\varepsilon_y})_E^+ = -(A_{\varepsilon_y})_E$	(A6)

In Eqs. (A4) and (A5), the terms with the subscript ‘‘BC’’ are imposed from given inflow boundary values, and when doing so for  $k_{BC}$  and  $\varepsilon_{BC}$ , pre-processing is required from the given (test-specific) inflow values. The pre-processing is based on Eq. (A7) in which  $I$  is the turbulence intensity and  $D_r$  is the turbulent viscosity ratio (Cea 2005).

$$\begin{aligned}
k_{BC} &= \frac{3}{2} (I \sqrt{u_{BC} u_{BC} + v_{BC} v_{BC}})^2 \\
\varepsilon_{BC} &= \frac{c_\mu k^2}{D_m D_r}, \quad D_r = D_t / D_m
\end{aligned} \tag{A7}$$

According to Ginting (2019) and Lutsenko (2017),  $I$  should be lower than 0.01 for low-turbulent flow, between 0.01 to 0.05 for medium-turbulent flow, and between 0.05 to 0.2 for high-turbulent flow, while  $D_r$  should be lower than 10. Since all the simulated test cases (Secs. 3 and 4) have a (subcritical, low-turbulence) inflow that is far from the turbulence production region,  $I = 0.01$  and  $D_r = 0.1$  were used – but our numerical experiments show that using up to 10-fold higher values for  $I$  and  $D_r$  leads to very similar results (not shown).

### A.2. Scalable wall function (ScWF)

Because the  $k$ - $\varepsilon$  model's two transport equations are based on the fully turbulent assumption, they may not be valid at the near-dry-wall cells: the wet cells including at least one wet-dry front, which are adjacent to the dry cells representing unsubmerged topographies. At these cells, a laminar wall-boundary layer should be imposed based on the ScWF (Ginting and Ginting 2019) to correct  $(U_{\text{turb}_i}^K)_{i=1,2}$ . For example, assuming the wet sample cell is neighboured by an eastern dry-wall cell (Fig. 1), the ScWF uses the velocity's average component  $v^0$  (tangential to dry-wall cell) to produce the wall-friction velocity  $w_p^*$  based on the iterative procedure reported in Ginting and Ginting (2019). The calculated  $w_p^*$  is then used to correct  $(U_{\text{turb}_i}^0)_{i=1,2}$ , following Eq. (A8), while imposing zero values for the slope coefficients  $[(U_{\text{turb}_i}^{1x})_{i=1,2} = (U_{\text{turb}_i}^{1y})_{i=1,2} = 0]$ :

$$\begin{aligned}
U_{\text{turb}_1}^0 &= h^0 \frac{(w_p^*)^2}{\sqrt{c_\mu}} \\
U_{\text{turb}_2}^0 &= 2h^0 \frac{(w_p^*)^3}{0.4\Delta x}
\end{aligned} \tag{A8}$$

### A.3. Cellwise evaluation of the source terms

The evaluation of the components of in  $(S_{\text{mean}_i}^K)_{i=1,2,3}$ , is achieved cellwise from the DG2 approximation (Eq. 11): using revised degrees of freedom (the mean-flow variable and of the topography) from the wet-dry front treatments when integrating a topography source term component, and stability-preserving integration for a friction source term component (Shaw et al. 2021). Whereas  $(S_{\text{turb}_i}^K)_{i=1,2}$  are evaluated as:

$$\begin{aligned}
S_{\text{turb}_i}^0 &= (S_{\text{turb}_i})_C \\
S_{\text{turb}_i}^{1x} &= \frac{1}{2} [(S_{\text{turb}_i})_{Gx2} - (S_{\text{turb}_i})_{Gx1}] \\
S_{\text{turb}_i}^{1y} &= \frac{1}{2} [(S_{\text{turb}_i})_{Gy2} - (S_{\text{turb}_i})_{Gy1}]
\end{aligned} \tag{A9}$$

## Acknowledgement

This work was supported by the UK Engineering and Physical Sciences Research Council (EPSRC) grant EP/R007349/1. It is part of the SEAMLESS-WAVE project (SoftwarE infrAstructure for Multi-purpose fLood modElling at various scaleS based on WAVElets, <https://www.seamlesswave.com>). For the purpose of open access, the author has applied a Creative Commons Attribution (CC BY) licence to any Author Accepted Manuscript version arising.

## Declaration of competing interest

The authors declare that they have no known competing financial interests or personal relationships that could have appeared to influence the work reported in this paper.

## Data and software availability

The code, and some of the data, generated or used during the study are available in a repository or online in accordance with funder data retention policies. The code of the DG2-RANS- $k-\epsilon$  turbulent flow solver and the DG2-RANS laminar flow solver was programmed on the LISFLOOD-FP hydraulic modelling environment, in a dedicated open-source release available in a Zenodo repository: <https://doi.org/10.5281/zenodo.7628739>. The repository also includes the (test-specific) raster-formatted files of the DG2 approximation data of ground elevations and initial flow conditions (Sec. 3.1), for reproducing the simulations (Sec. 4). Details on the setting up and running this code is on [https://www.seamlesswave.com/DG2\\_RANS](https://www.seamlesswave.com/DG2_RANS), with demonstration videos of the DG2-RANS- $k-\epsilon$  turbulent flow solver's performance during the simulations (videos linked to test-case images, on [https://www.seamlesswave.com/DG2\\_RANS](https://www.seamlesswave.com/DG2_RANS)). Note that downloading, building, setting up and running the DG2-RANS- $k-\epsilon$  turbulent flow solver follows the standard procedure on LISFLOOD-FP (version 8 and above) that is described on <https://www.seamlesswave.com/LISFLOOD8.0> and with step by step guidance in a series of video supplements (e.g., <https://zenodo.org/records/6685125>).

## CRedit authorship contribution statement

**Georges Kesserwani:** conceived and wrote the paper; Funding acquisition, Conceptualization, Validation, Supervision, Formal analysis, Writing – original draft. **Xitong Sun:** conducted the comparative analysis; Formal analysis, Investigation, Visualisation, Writing – review & editing. **Mahya Hajihassanpour:** formulated and coded the DG2-RANS- $k-\epsilon$  solver (CPU version) with preliminary analysis of simulation results; Methodology, Software, Visualisation, Data curation, Resources, Writing – review & editing. **Mohammad Kazem Sharifian:** coded the DG2-RANS- $k-\epsilon$  solver (GPU version); Software, Data curation.

## References

- Abakouy, A., E. M. Chaabelasri, N. Salhi, and I. Elmahi (2017), An enhanced finite volume method for numerical simulation of turbulent shallow water flows, *Journal of Materials and Environmental Sciences*, Vol. 8, No. 5, 1708-1717.
- Ayog, J. L., G. Kesserwani, J. Shaw, M. K. Sharifian, and D. Bau (2021), Second-order discontinuous Galerkin flood model: Comparison with industry-standard finite volume models, *Journal of Hydrology*, Vol 594, 125924.
- Babarutsi, S., J. G., and V. H. Chu (1989), Experimental investigation of shallow recirculating flows, *Journal of Hydraulic Engineering*, Vol. 115, No. 7, 906-924.
- Bazin, P.-H., E. Mignot, and A. Paquier (2017), Computing flooding of crossroads with obstacles using a 2D numerical model, *Journal of Hydraulic Research*, Vol. 55, No. 1, 72-84.
- Begnudelli, L., Alessandro V., and B. F. Sanders (2010), A balanced treatment of secondary currents, turbulence and dispersion in a depth-integrated hydrodynamic and bed deformation model for channel bends, *Advances in Water Resources*, Vol. 33, No. 1, 17-33.
- Bergmann, M., Morsbach, C., Franke, M. (2019). Implicit LES of a Turbulent Channel Flow with High-Order Discontinuous Galerkin and Finite Volume Discretization. In: Salvetti, M., Armenio, V., Fröhlich, J., Geurts, B., Kuerten, H. (eds) *Direct and Large-Eddy Simulation XI*. ERCOFTAC Series, vol 25. Springer, Cham. [https://doi.org/10.1007/978-3-030-04915-7\\_9](https://doi.org/10.1007/978-3-030-04915-7_9)
- Bonev, B., J. S. Hesthaven, F. X. Giraldo, and M. A. Koper (2018), Discontinuous Galerkin scheme for the spherical shallow water equations with applications to tsunami modeling and prediction, *Journal of Computational Physics*, 362, 425-448.
- Cea, L. (2005), An unstructured finite volume model for unsteady turbulent shallow water flow with wet-dry fronts: numerical solver and experimental validation, *Universidade da Coruna*.

- Cea, L., J. Puertas, and M. E. Vázquez-Cendón (2007), Depth Averaged Modelling of Turbulent Shallow Water Flow with Wet-Dry Fronts, *Archives of Computational Methods in Engineering*, Vol. 14, No. 3, 303-341.
- Cea, L., J. R. French, and M. E. Vázquez-Cendón (2006), Numerical modelling of tidal flows in complex estuaries including turbulence: an unstructured finite volume solver and experimental validation, *International Journal for Numerical Methods in Engineering*, Vol. 67, No. 13, 1909-1932.
- Cockburn, B., and C.-W. Shu (1998), The local discontinuous Galerkin method for time-dependent convection-diffusion systems, *SIAM Journal on Numerical Analysis*, Vol. 35, No. 6, 2440-2463.
- Cockburn, B., and C. W. Shu (2001), Runge–Kutta Discontinuous Galerkin Methods for Convection-Dominated Problems, *Journal of Scientific Computing*, Vol. 16, No. 3, 173-261.
- Corredor-Garcia, J., A. Delalande, V. Stovin, and I. Guymer (2021), Surface Velocity Fields from Experiments in Flow Through Emergent Vegetation (Version 1) [Data Set], *the University of Sheffield*, <https://doi.org/10.15131/shef.data.16550388>.
- Dewals, B., V. Kitsikoudis, M. A. Mejía-Morales, P. Archambeau, E. Mignot, S. Proust, S. Erpicum, M. Piroton, and A. Paquier (2023), Can the 2D shallow water equations model flow intrusion into buildings during urban floods?, *Journal of Hydrology*, Vol. 619, 129231.
- Dairay, T., E. Lamballais, S. Laizet, and J. C. Vassilicos (2017), Numerical dissipation vs. subgrid-scale modelling for large eddy simulation, *Journal of Computational Physics*, Vol. 337, 252-274.
- Ginting, B. M. (2019), Central-upwind scheme for 2D turbulent shallow flows using high-resolution meshes with scalable wall functions, *Computers & Fluids*, Vol. 179, 394-421.
- Ginting, B. M., and H. Ginting (2019), Hybrid Artificial Viscosity–Central-Upwind Scheme for Recirculating Turbulent Shallow Water Flows, *Journal of Hydraulic Engineering*, Vol. 145, No. 12, 04019041.
- Gioia, G., and F. A. Bombardelli (2001), Scaling and similarity in rough channel flows, *Physical review letters*, Vol. 88, No. 1, 014501.

Gorji, S., M. Seddighi, C. Ariyaratne, A. E. Vardy, T. O'Donoghue, D. Pokrajac, and S. He. (2014), A comparative study of turbulence models in a transient channel flow, *Computers & Fluids*, Vol. 89, 111-123.

Hajihassanpour, M., and K. Hejranfar (2020), A high-order nodal discontinuous Galerkin method to solve preconditioned multiphase Euler/Navier-Stokes equations for inviscid/viscous cavitating flows, *International Journal for Numerical Methods in Fluids*, Vol. 92, No. 5, 478-508.

Hajihassanpour, M., and K. Hejranfar (2022), A high-order nodal discontinuous Galerkin method for simulation of three-dimensional non-cavitating/cavitating flows, *Finite Elements in Analysis and Design*, Vol. 200, 103681.

Hajihassanpour, M., G. Kesserwani, and M. K. Sharifian (2024), DG2-RANS k- $\epsilon$  turbulence simulator on LISFLOOD-FP, *Zenodo*, <https://doi.org/10.5281/zenodo.7628739>.

Haun, S., N. R. B. Olsen, and R. Feurich (2011), Numerical modeling of flow over trapezoidal broad-crested weir, *Engineering Applications of Computational Fluid Mechanics*, Vol. 5, No. 3, 397-405.

Hejranfar, K., and M. Hajihassanpour (2017), A high-order nodal discontinuous Galerkin method for solution of compressible non-cavitating and cavitating flows, *Computers & Fluids*, Vol. 156, 175-199.

Hesthaven, J. S., and T. Warburton (2007), Nodal discontinuous Galerkin methods: algorithms, analysis, and applications, *Springer*.

Hinterberger, C., J. Fröhlich, and W. Rodi (2007), Three-dimensional and depth-averaged large-eddy simulations of some shallow water flows, *Journal of Hydraulic Engineering*, Vol. 133, No. 8, 857-872.

Hou, J., Q. Liang, F. Simons, and R. Hinkelmann (2013), A stable 2D unstructured shallow flow model for simulations of wetting and drying over rough terrains, *Computers & Fluids*, Vol. 82, 132-147.

Jamei, M., A. Raeisi Isa Abadi, and I. Ahmadianfar (2019), A Lax–Wendroff-IMPES scheme for a two-phase flow in porous media using interior penalty discontinuous Galerkin method, *Numerical Heat Transfer, Part B: Fundamentals*, Vol. 75, No. 5, 325-346.

- Jha, S. K., and F. A. Bombardelli (2011), Theoretical/numerical model for the transport of non-uniform suspended sediment in open channels, *Advances in water resources*, Vol. 34, No. 5, 577-591.
- Jin, T., P. X. Ramos, E. Mignot, N. Riviere, and T. De Mulder (2023), On the delineation of the flow separation zone in open-channel confluences, *Advances in Water Resources*, Vol. 180, 104525.
- Kärnä, T., Kramer, S. C., Mitchell, L., Ham, D. A., Piggott, M. D., and Baptista, A. M. (2018), Thetis coastal ocean model: discontinuous Galerkin discretization for the three-dimensional hydrostatic equations, *Geoscientific Model Development*, Vol. 11, No. 11, 4359-4382.
- Kärnä, T. (2020), Discontinuous Galerkin discretization for the two-equation turbulence closure model, *Ocean Modelling*, Vol. 150, 101619.
- Kesserwani, G. (2013), Topography discretization techniques for Godunov-type shallow water numerical models: a comparative study, *Journal of Hydraulic Research*, Vol. 51, No. 4, 351-367.
- Kesserwani, G., and Q. Liang (2012), Locally limited and fully conserved RKDG2 shallow water solutions with wetting and drying, *Journal of Scientific Computing*, Vol. 50, No. 3, 120-144.
- Kesserwani, G., and Y. Wang (2014), Discontinuous Galerkin flood model formulation: Luxury or necessity?, *Water Resources Research*, Vol. 50, No. 8, 6522-6541.
- Kesserwani, G., and M. K. Sharifian (2020), (Multi)wavelets increase both accuracy and efficiency of standard Godunov-type hydrodynamic models: Robust 2D approaches, *Advances in Water Resources*, Vol. 144, 103693.
- Kesserwani, G., J. L. Ayog, and D. Bau (2018), Discontinuous Galerkin formulation for 2D hydrodynamic modelling: Trade-offs between theoretical complexity and practical convenience, *Computer Methods in Applied Mechanics and Engineering*, Vol. 342, 710-741.
- Kesserwani, G., J. L. Ayog, M. K. Sharifian, and D. Bau (2023), Shallow-flow velocity predictions using discontinuous Galerkin solutions, *Journal of Hydraulic Engineering*, Vol. 149, No. 5, 04023008.

- Krivodonova, L., J. Xin, J. F. Remacle, N. Chevaugeon, and J. E. Flaherty (2004), Shock detection and limiting with discontinuous Galerkin methods for hyperbolic conservation laws, *Applied Numerical Mathematics*, Vol. 48, No. 3, 323-338.
- Kesserwani, G., R. Ghostine, J. Vazquez, A. Ghenaim, and R. Mose (2008), Riemann solvers with Runge-Kutta discontinuous Galerkin schemes for the 1D shallow water equations, *Journal of Hydraulic Engineering*, Vol. 134, No. 2, 243-255.
- Komen, E.M.J., L.H. Camilo, A. Shams, B.J. Geurts, and B. Koren (2017), A quantification method for numerical dissipation in quasi-DNS and under-resolved DNS, and effects of numerical dissipation in quasi-DNS and under-resolved DNS of turbulent channel flows, *Journal of Computational Physics*, Vol. 345, 565-595.
- Landmann, B., M. Kessler, S. Wagner, and E. Krämer (2008), A parallel, high-order discontinuous Galerkin code for laminar and turbulent flows, *Computers & Fluids*, Vol. 37, No. 4, 427-438.
- Lee, H. (2021), Discontinuous Galerkin discretization of shallow water equations in implicit primal formulations for turbulent stresses, *Journal of Mechanical Science and Technology*, Vol. 35, 2471-2479.
- Li, C. W., and C. Zeng (2009), 3D Numerical modelling of flow divisions at open channel junctions with or without vegetation, *Advances in Water Resources*, Vol. 32, No. 1, 49-60.
- Liang, Q., and F. Marche (2009), Numerical resolution of well-balanced shallow water equations with complex source terms, *Advances in water resources*, Vol. 32, No. 6, 873-884.
- Ling, D., C. W. Shu, and W. Yan (2023), Local discontinuous Galerkin methods for diffusive–viscous wave equations, *Journal of Computational and Applied Mathematics*, Vol. 419, 114690.
- Lloyd, P. M., and P. K. Stansby (1997a), Shallow-water flow around model conical islands of small side slope II: Submerged, *Journal of Hydraulic Engineering*, Vol. 123, No. 12, 1068-1077.
- Lloyd, P. M., and P. K. Stansby (1997b), Shallow-water flow around model conical islands of small side slope I: Surface piercing, *Journal of Hydraulic Engineering*, Vol. 123, No. 12, 1057-1067.

Lohry, M. W., and L. Martinelli (2021), On the development, verification, and validation of a discontinuous Galerkin solver for the Navier–Stokes equations, *Computers & Fluids*, Vol. 223, 104921.

Lutsenko, I., M. Serikbay, A. Akiltayev, L. R. Rojas-Solórzano and Y. Zhao (2017), Effect of Free-Stream Turbulence Intensity on Transonic Airfoil with Shock Wave, *In IOP Conference Series: Materials Science and Engineering*, Vol. 234, No. 1, 012016.

Macías, J., M. J. Castro, and C. Escalante (2020), Performance assessment of the Tsunami-HySEA model for NTHMP tsunami currents benchmarking. Laboratory data, *Coastal Engineering*, Vol. 158, 103667.

Mignot, E., and W. Brevis (2020), Coherent turbulent structures within open-channel lateral cavities, *Journal of Hydraulic Engineering*, Vol. 146, No. 2, 04019066.

Mignot, E., C. Zeng, G. Dominguez, C.-W. Li, N. Rivière, and P.-H. Bazin (2013), Impact of topographic obstacles on the discharge distribution in open-channel bifurcations, *Journal of hydrology*, Vol. 494, 10-19.

Miller, C. T., C. N. Dawson, M. W. Farthing, T. Y. Hou, J. Huang, C. E. Kees, C. T. Kelley, and H. Petter Langtangen (2013), Numerical simulation of water resources problems: Models, methods, and trends, *Advances in Water Resources*, Vol. 51, 405-437.

Moura R.C., G. Mengaldo, J. Peiró, and S. J. Sherwin (2017). On the eddy-resolving capability of high-order discontinuous Galerkin approaches to implicit LES / under-resolved DNS of Euler turbulence. *Journal of Computational Physics*, Vol. 330, 615-623.

Navas-Montilla, A., C. Juez, M. J. Franca, and J. Murillo (2019), Depth-averaged unsteady RANS simulation of resonant shallow flows in lateral cavities using augmented WENO-ADER schemes, *Journal of Computational Physics*, Vol. 395, 511-536.

Neary, V. S., and A. J. Odgaard (1993), Three-dimensional flow structure at open-channel diversions, *Journal of Hydraulic Engineering*, Vol. 119, No. 11, 1223-1230.

Ninto, Y., and M. H. Garcia (1966), Experiments on particle-turbulence interactions in the near-wall region of an open channel flow: implications for sediment transport, *Journal of Fluid Mechanics*, Vol. 326, 285-319.

- Pandey, A. K., and P. K. Mohapatra (2023), Flow Dynamics and Pollutant Transport at an Artificial Right-Angled Open-Channel Junction with a Deformed Bed, *Journal of Hydraulic Engineering*, Vol. 149, No. 4, 04023006.
- Plata, M. L., V. Couaillier, and M.-C. Pape (2018). On the use of a high-order discontinuous Galerkin method for DNS and LES of wall-bounded turbulence. *Computers and Fluids*, Vol. 176, 320-337.
- Qu, L., C. Norberg, L. Davidson, S.-H. Peng, and F. Wang (2013), Quantitative numerical analysis of flow past a circular cylinder at Reynolds number between 50 and 200, *Journal of Fluids and Structures*, Vol. 39, 347-370.
- Rajani, B. N., A. K., and S. M. (2009), Numerical simulation of laminar flow past a circular cylinder, *Applied Mathematical Modelling*, Vol. 33, No. 3, 1228-1247.
- Ramamurthy, A. S., J. Qu, and D. Vo (2007), Numerical and experimental study of dividing open-channel flows, *Journal of Hydraulic Engineering*, Vol.133, No. 10, 1135-1144.
- Rastogi, A. K., and W. Rodi (1978), Predictions of heat and mass transfer in open channels, *Journal of the Hydraulics division*, Vol. 104, No. 3, 397-420.
- Rodi, W. (2017), Turbulence modeling and simulation in hydraulics: A historical review, *Journal of Hydraulic Engineering*, Vol. 143, No. 5, 03117001.
- Rodi, W. (1993), Turbulence models and their application in hydraulics, *Routledge*.
- Rubinato, M. (2015), Physical scale modelling of urban flood systems (Ph.D. thesis), Department of Civil and Structural Engineering, *the University of Sheffield*.
- Rubinato, M., J. Shucksmith, R. Martins, and G. Kesserwani (2021), Particle image velocimetry (PIV) dataset for the parking lot configuration with a closed manhole, *Zenodo*, <https://doi.org/10.5281/zenodo.4596731>.
- Sen, S., S. Mittal, and G. Biswas (2011), Flow past a square cylinder at low Reynolds numbers, *International Journal for Numerical Methods in Fluids*, Vol. 67, No. 9, 1160-1174.

Sharifian, M. K., G. Kesserwani, and Y. Hassanzadeh (2018), A discontinuous Galerkin approach for conservative modeling of fully nonlinear and weakly dispersive wave transformations, *Ocean Modelling*, Vol. 125, 61-79.

Shaw, J., G. Kesserwani, J. Neal, P. Bates, and M. K. Sharifian (2021), LISFLOOD-FP 8.0: the new discontinuous Galerkin shallow-water solver for multi-core CPUs and GPUs, *Geoscientific Model Development*, Vol. 14, No. 6, 3577-3602.

Shettar, A. S., and K. K. Murthy (1996), A numerical study of division of flow in open channels, *Journal of Hydraulic Research*, Vol. 34, No. 5, 651-675.

Shinneeb, A. M., G. Nasif, and R. Balachandar (2021), Effect of the aspect ratio on the velocity field of a straight open-channel flow, *Physics of Fluids*, Vol. 33, No. 8.

Shucksmith, J. D., J. B. Boxall, and I. Guymer (2010), Effects of emergent and submerged natural vegetation on longitudinal mixing in open channel flow, *Water Resources Research*, Vol. 46, No. 4.

Sun, X., G. Kesserwani, M. K. Sharifian, and V. Stovin (2023), Simulation of laminar to transitional wakes past cylinders with a discontinuous Galerkin inviscid shallow water model, *Journal of Hydraulic Research*, Vol. 61, No. 5, 631-650.

Toro, E. F. (2010), Riemann solvers and numerical methods for fluid dynamics: a practical introduction, *Springer*.

Toro, E. F., and P. Garcia-Navarro (2007), Godunov-type methods for free-surface shallow flows: A review, *Journal of Hydraulic Research*, Vol. 45, No. 6, 736-751.

Vázquez-Cendón, M. E., L. Cea, and J. Puertas (2009), The shallow water model: The relevance of geometry and turbulence, *Monografías de la Real Academia de Ciencias de Zaragoza*, Vol. 31, 217-236.

Wei, L., and Y. Xia (2024), An indicator-based hybrid limiter in discontinuous Galerkin methods for hyperbolic conservation laws, *Journal of Computational Physics*, Vol. 498, 112676.

Wu, W. (2004), Depth-averaged two-dimensional numerical modeling of unsteady flow and nonuniform sediment transport in open channels, *Journal of hydraulic engineering*, Vol. 130, No. 10, 1013-1024.

Yu, C., and J. Duan (2012), Two-dimensional depth-averaged finite volume model for unsteady turbulent flow, *Journal of hydraulic research*, Vol. 50, No. 6, 599-611.

Zhang, D., A. Rinoshika, Y. Zheng, Z. Li, and Y. Zhang (2022), Turbulent flow structures around a wavy square cylinder based on large eddy simulation, *Fluid Dynamics*, Vol. 57, No. 1, 96-110.

Zhang, Y., M. Rubinato, E. Kazemi, J. H. Pu, Y. Huang, and P. Lin (2019), Numerical and experimental analysis of shallow turbulent flow over complex roughness beds, *International Journal of Computational Fluid Dynamics*, Vol. 33, No. 5, 202-221.

Zou, P. X., J. D. Bricker, and W. SJ Uijtewaal (2020), Impacts of extreme events on hydrodynamic characteristics of a submerged floating tunnel, *Ocean Engineering*, Vol. 218, 108221.

Zou, P., T. Kim, J. D. Bricker, and W. SJ Uijtewaal (2023), Assessment of interfacial turbulence treatment models for free surface flows, *Journal of Hydraulic Research*, Vol. 61, No. 5, 651-667.